Check for updates

ChemBioChem

Chemistry Europe
European Chemical Societies Publishing
ChemBioChem

RESEARCH ARTICLE OPEN ACCESS

Uracil–Peptide–Pyrene Conjugates as Cu^{2+}-Sensitive Probes Targeting DNA, RNA, and Biorelevant Model Membranes

Dijana Pavlović Saftić[1] | Lucija Lulić Horvat[2] | Ivo Piantanida[1]

[1]Division of Organic Chemistry and Biochemistry, Ruđer Bošković Institute, Zagreb, Croatia | [2]Division of Molecular Biology, Ruđer Bošković Institute, Zagreb, Croatia

Correspondence: Dijana Pavlović Saftić (Dijana.Pavlovic.Saftic@irb.hr)

Received: 15 December 2025 | **Revised:** 6 March 2026 | **Accepted:** 11 March 2026

Keywords: 1,2,3-triazole–uracil conjugates | copper(II) metal–ligand interactions | DNA/RNA fluorescent probes | pyrene-based fluorophores | theranostic agents

ABSTRACT

We report a series of uracil-triazole–pyrene peptidomimetics (**2**–**4**) designed to achieve modular geometric control through peptide linkers of varying length and flexibility. All three compounds exhibited submicromolar affinity for ds-DNA, while compound **4** also showed strong binding to ds-RNA, demonstrating the advantage of combining a uracil recognition unit with an extended pyrene aromatic surface compared to the **Pyr-Trp** reference ligand and the phenanthridine analog **4′**. Structural variations strongly affected Cu(II) coordination. Although **Pyr-Trp** bound Cu(II) approximately 1000-fold more strongly than the short, rigid compound **2**, elongation and increased linker flexibility restored high affinity in **4**. Notably, replacing phenanthridine (**4′**) with pyrene (**4**) enhanced Cu(II) binding by nearly 100-fold, highlighting the superior coordination properties of the pyrene scaffold. Cu(II) complexation significantly enhanced nucleic acid binding exclusively for compound **2**, increasing its DNA/RNA affinity 15-fold. The resulting **2**–Cu(II) complex displayed exceptional selectivity for poly rA–poly rU, exceeding that of the **Pyr-Trp**–Cu(II) analog by more than 10-fold, consistent with uracil-mediated Hoogsteen-type recognition. Membrane interactions with POPC MLVs were linker-dependent, producing fluorescence enhancements of up to 1400% (**2**), 650% (**3**), and 100% (**4**). Together with negligible cytotoxicity, these findings indicate that compounds **2**–**4** represent promising multifunctional platforms for Cu^{2+} sensing and photoinduced therapeutic applications.

1 | Introduction

Small molecules capable of recognizing specific DNA or RNA sequences have been extensively studied, with many examples demonstrating selective recognition of multinucleobase motifs in duplex and single-stranded nucleic acids [1–3]. Strategies such as modular assembly, groove binding, and intercalation have enabled targeting of longer motifs. However, discriminating single nucleobases or short homologous runs remains challenging due to minimal structural and energetic differences, strong solvation effects, and nucleic acid dynamics. Efficient recognition of abasic sites [4] and short homologous nucleobase runs in DNA [5–8] and RNA [9, 10] has thus remained an active research focus [11], with implications for nucleic acid stability, molecular recognition, and genetic fidelity.

Our previous work with phenanthridinium- and bis-phenanthridinium–nucleobase conjugates [12–20] demonstrated selective DNA/RNA recognition through aromatic stacking and hydrogen bonding between ligand and complementary nucleobases. Peptide-based linkers were employed for modular assembly, and because short peptides can interact with polynucleotides [14, 21–26], often incorporating 1,2,3-triazoles via click chemistry [27]. Triazoles offer chemical stability, low toxicity, and therapeutic potential (anticancer [28], antibacterial [29], antifungal [30, 31], antitubercular [32], antiviral [33]), and can interact with nucleic acids via hydrogen bonding, dipole–dipole, and π–π stacking. They also coordinate biorelevant cations, especially Cu^{2+}, which can modulate binding modes, thermal stabilization, and higher-order architectures in intercalator–peptide scaffolds [3, 21, 33–36].

This is an open access article under the terms of the Creative Commons Attribution-NonCommercial-NoDerivs License, which permits use and distribution in any medium, provided the original work is properly cited, the use is non-commercial and no modifications or adaptations are made.

© 2026 The Author(s). *ChemBioChem* published by Wiley-VCH GmbH.

Recently, uracil-triazole-phenanthridine analogs **3′** and **4′**, and building block **1** [14], showed at least 10-fold higher affinity than aliphatic analogs, with lysine-containing **4′** selective for poly rA–poly rU and poly U. Inspired by pyrene-peptide conjugates targeting DNA/RNA and membranes [36–38], we replaced phenanthridine with pyrene, preparing uracil–triazole–pyrene analogs **2–4** (Scheme 1) to exploit pyrene's extended aromatic surface for stronger stacking and enhanced membrane incorporation. We also studied Cu^{2+} binding and the affinity of ligands and their complexes for selected ds-DNA/RNA and ss-RNA targets.

Polynucleotide models used included common ds-DNA representatives with defined structures (Table S4): *ct*DNA (B-helical, balanced A-T/G-C), poly(dAdT)$_2$, and poly(dGdC)$_2$ (B-helical, with minor-groove steric hindrance in the latter), as well as ds-RNA poly rA–poly rU (A-helical) [39, 40]. Binding affinity was also assessed with ss-polynucleotides poly(U) and poly(A), complementary to the uracil conjugates 2–4. DNA/RNA interactions were mostly studied at pH 5.0, relevant to slightly acidic tumor tissue [41], where poly(A) undergoes a reversible transition to a parallel-stranded helix (poly AH$^+$–poly AH$^+$) via N1 protonation and reverse Hoogsteen pairing [42, 43], mimicking acidic compartments such as lysosomes and endosomes [44], with implications for DNA binding, endosomal protection, and compartment-specific recognition [45]. Studies with the POPC membrane model were conducted at physiological conditions (pH 7.0), with the aim of determining the affinity and fluorimetric response of the studied compounds bound to the lipidous multilayer membrane. Namely, studied compounds consist of a strongly hydrophobic pyrene fluorophore (commonly used for membrane imaging) coupled with peptide uracil tails rich in a hydrogen bonding pattern. Latter could be potentially used by several membrane-transporters, such as SLC15 family facilitating electrogenic symport of di/tripeptides and peptidomimetics using the proton gradient [46], or uracil-specific transporters, such as bacterial UraA or eukaryotic FurE, which also operate as proton symporters in the NAT/NCS2 family [47].

2 | Results and Discussion

2.1 | Synthesis

Synthesis of 5-(1,2,3-triazol-4-yl)uracil-pyrene conjugates **2–4** was carried out as shown in Scheme 2. In the first step, liquid-phase peptide coupling of amine **A**, which was synthesized earlier [14], with commercially available 1-pyrenebutyric acid (PBA) was performed using *N*,*N*,*N*,*N*-tetramethyl-O-(1*H*-benzotriazol-1-yl) uronium hexafluorophosphate (HBTU) as the coupling reagent, 1-hydroxybenzotriazole (HOBT) as a coupling additive that significantly reduces racemization, and triethylamine (TEA) in dry acetonitrile, producing conjugate **2** in 42% yield. Meanwhile, trifluoroacetate salt **1**, obtained from amine **A** as described previously [14], was reacted with PBA using the same HBTU/HOBT

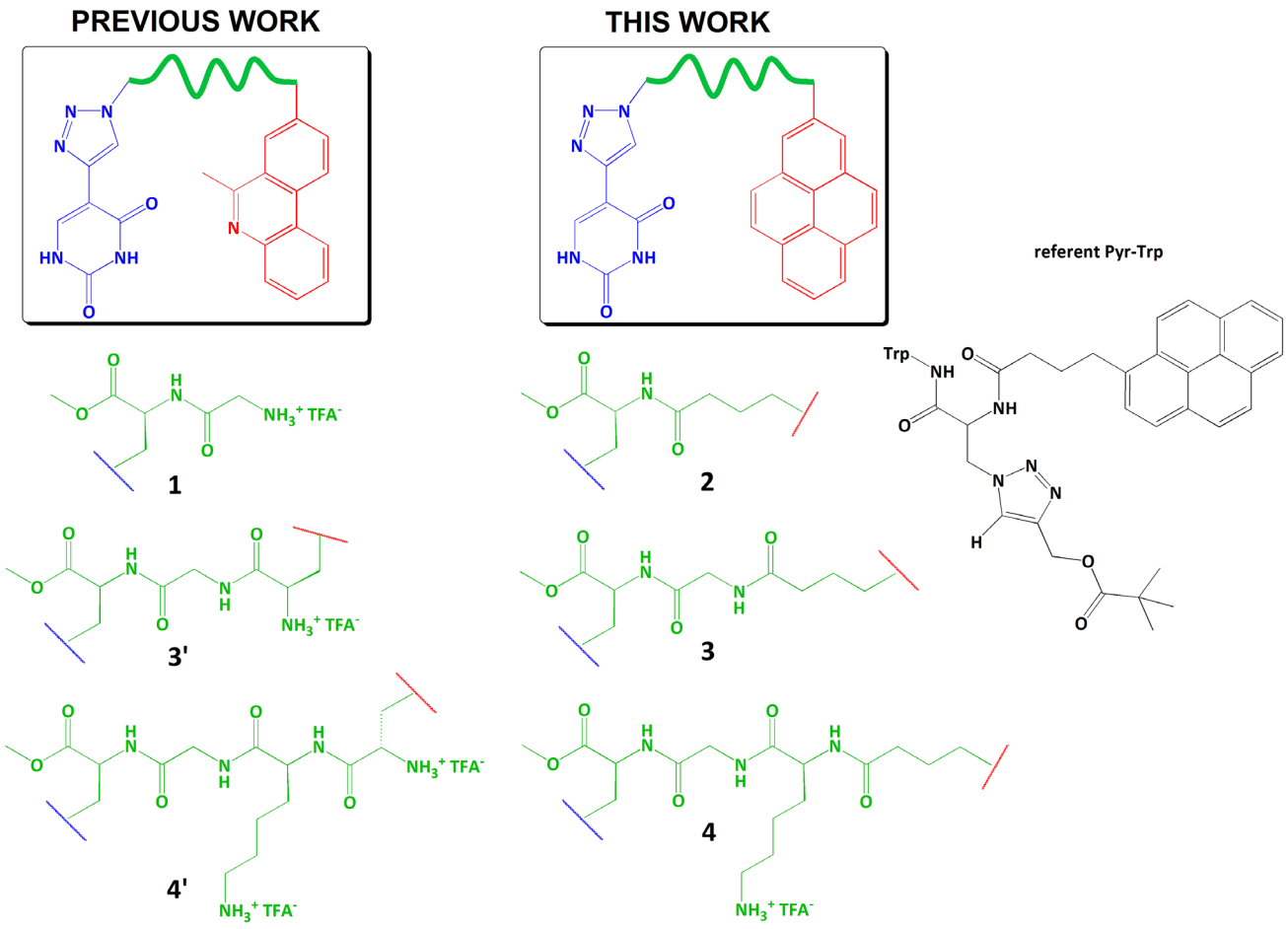

SCHEME 1 | General structures of previously reported derivatives **3′** and **4′** with reference compound **1** [14], and here studied analogs **2**, **3**, and **4**, and comparison with previously studied analog of ligand **2** (**Pyr-Trp**) [36].

14397633, 2026, 8, Downloaded from https://chemistry-europe.onlinelibrary.wiley.com/doi/10.1002/cbic.70312 by Ruder Boskovic Institute, Wiley Online Library on [25/11/2026]. See the Terms and Conditions (https://onlinelibrary.wiley.com/terms-and-conditions) on Wiley Online Library for rules of use; OA articles are governed by the applicable Creative Commons License

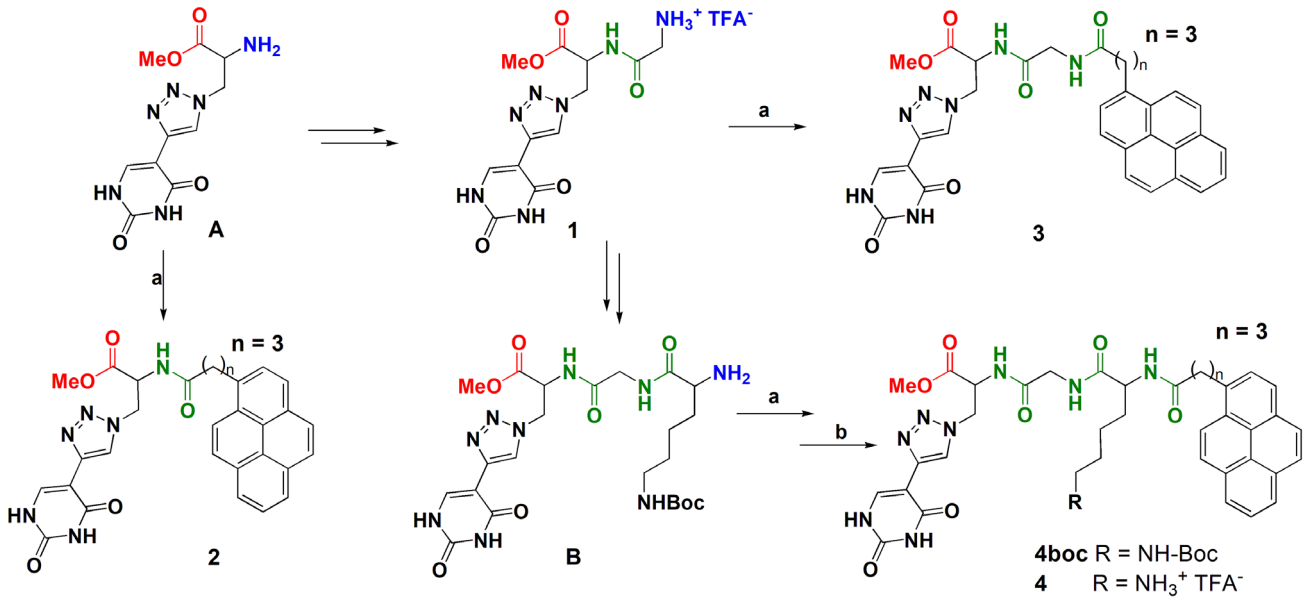

SCHEME 2 | Synthesis of peptidomimetics **2–4** with pyrene and triazolyluracilyl-L-alanine side chains. Reagents and conditions: (a) PBA, Et_3N, HOBT, HBTU, dry CH_3CN, r.t., overnight. (b) TFA/CH_2Cl_2 1:1, r.t., overnight.

and TEA protocol in dry acetonitrile, resulting in the final conjugate **3** with a 63% yield. Next, the peptide coupling of tripeptide **B**, synthesized as previously reported [14], with PBA yielded peptidomimetic **4boc** in 47% yield. Acid hydrolysis of **4boc** with a mixture of trifluoroacetic acid/dichloromethane (TFA/DCM) in a 1:1 ratio produced the desired trifluoroacetate salt **4**, quantitatively.

2.2 | Photophysical and Spectrophotometric Properties of the Novel Compounds

The compounds were dissolved in dimethyl sulfoxide at a concentration of 10 mM. Stock solutions were stored at 4°C, while working aliquots were kept at 25°C. No visible precipitation was observed in the working solutions under these conditions. Preliminary spectroscopic characterization of peptidomimetics **2–4** was carried out in sodium cacodylate buffer (pH 5), under conditions analogous to those previously established for related structural analogs [14]. Under the experimental conditions used, the absorbance intensities of investigated compounds **2–4** were linearly dependent on concentration up to $c = 2 \times 10^{-5}$ M (Figures S11–S13), allowing for the reliable determination of molar absorption coefficients (ε; Table 1). For comparison, the spectrophotometric data of the previously reported derivative **1** (Figure S14) [14], utilized as the synthetic precursor for compounds **3** and **4**, are included. The Stokes shifts of the newly synthesized derivatives are approximately similar to each other (Table 1) and show negligible differences compared to the reference compound PBA. In contrast, the molar absorption coefficients of the studied compounds differ significantly, with values roughly half of those obtained for PBA. Furthermore, the fluorescence quantum yield of derivative **2**, measured relative to the reference compound PBA in aqueous medium (sodium cacodylate buffer, pH 7), is negligible, indicating inefficient radiative decay and the presence of nonradiative relaxation pathways or quenching effects that reduce its fluorescence efficiency. Due to the very similar intrinsic spectroscopic features of derivatives **3** and **4**, measurement of their fluorescence quantum yields was considered redundant.

TABLE 1 | Spectrophotometric data of 2–4 and references 1. Measurements were performed in sodium cacodylate buffer (pH 5.0 or pH 7.0, $I = 0.05$ M).

Compound	λ_{Abs}[a]/nm ($\varepsilon \times 10^3/M^{-1}\,cm^{-1}$)				$^{max}\lambda_{Em}$[a,b]/ nm (λ_{Exc})	$\Delta\lambda$[c]/ nm	Φ_F (λ_{Exc}/nm)
1	/	286 (10.3 ± 0.2)	/	/	/	/	/
2	275 (34.6 ± 0.6)	/	328 (19.3 ± 0.2)	344 (23.8 ± 0.5)	379 (275)	35	(4.66 ± 0.7) × 10^{-3} [d,e]
3	275 (36.0 ± 1.5)	/	328 (23.5 ± 0.9)	344 (30.0 ± 1.3)	378 (275)	34	/
4	276 (35.4 ± 0.1)	/	329 (21.5 ± 0.1)	345 (29.7 ± 0.1)	379 (276)	34	/
PBA	275 (59.4 ± 2.5)	/	326 (40 ± 0.7)	342 (55.3 ± 1.5)	379 (275)	37	0.15 ± 0.02[d,f]

[a]Measured in sodium cacodylate buffer (pH 5.0, $I = 0.05$ M). The extinction coefficient was determined from five data points; the reported error represents the deviation of the experimental values from the linear fit.
[b]The emission band of greatest intensity.
[c]Stokes shift.
[d]Measured in sodium cacodylate buffer (pH 7.0, $I = 0.05$ M).
[e]Fluorescence quantum yield measured by use of a reference compound (PBA). Error represents the standard deviation of three independent measurements.
[f]Literature [36].

14397633, 2026, 8, Downloaded from https://chemistry-europe.onlinelibrary.wiley.com/doi/10.1002/cbic.70312 by Ruder Boskovic Institute, Wiley Online Library on [25/11/2026]. See the Terms and Conditions (https://onlinelibrary.wiley.com/terms-and-conditions) on Wiley Online Library for rules of use; OA articles are governed by the applicable Creative Commons License

The absence of deviations from Beer–Lambert behavior indicates that no significant aggregation occurs under the tested conditions. However, a significant hypochromic effect was observed for **2–4** (Table 1, Figure 1) in comparison to PBA as a reference compound. Hypochromism results from Coulombic coupling between light-induced dipoles in adjacent chromophores, leading to diminished absorbance. The effect reflects both alignment of transition dipole moments and intramolecular π–π interactions [39, 48, 49]. Enhanced hypochromicity and the associated decrease in molar absorptivity (ε) are therefore indicative of molecular folding. In this case, the effect indicates intramolecular aromatic interactions involving pyrimidine, triazolyl, and pyrene units, although it does not provide a precise quantitative measure of interaction [50, 51].

Temperature-dependent absorption spectra of the investigated derivatives (Figure S15) demonstrated thermal stability upon heating up to 95°C and revealed near-complete spectral reproducibility upon cooling back to room temperature (25°C) (Table S3).

The fluorescence emission of compounds **2–4** exhibits modest changes within the 25°C–65°C range, showing a general trend of decreasing intensity with increasing temperature (Figures S16–S18). This behavior can be explained by the temperature-dependent enhancement of nonradiative relaxation pathways from the excited singlet state (S_1) to the ground state (S_o). Thermal energy facilitates vibrational relaxation and internal conversion, reducing the radiative emission. Upon cooling to room temperature, the emission of all compounds is reproducibly restored, with a slight enhancement relative to the initial preheating values, indicating a reversible modulation of the emissive excited states. Radiative emission is favored at lower temperatures, which can be attributed to the relative positioning of the two fluorophores within the molecule (uracil–triazole and pyrene). This effect is most pronounced for derivative **2**, where the mutual orientation and distance of the two fluorophoric units, ensured by the optimal linker length, allow the strongest intramolecular interactions, corresponding to the most favorable alignment of transition dipole moments and enhanced π–π interactions.

The newly synthesized derivatives are chiral molecules and are therefore expected to exhibit differential absorption of left- and right-circularly polarized light. This optical activity, measurable by circular dichroism (CD) spectroscopy, reflects the configuration and conformational preferences of the chiral fluorophoric units.

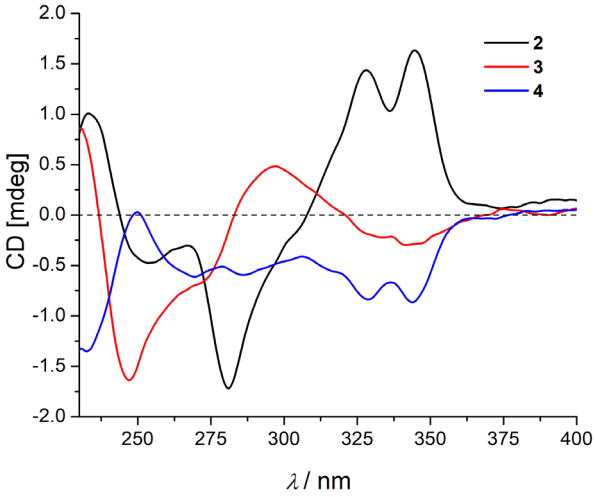

FIGURE 2 | Comparison of the CD spectra of the prepared derivatives **2–4**. Measurements were performed in sodium cacodylate buffer (pH 5.0, $I = 0.05$ M).

The CD spectra of compounds **2–4** are well resolved and exhibit pronounced differences in both band sign and position (Figure S19 and Figure 2), demonstrating efficient transfer of chirality from the amino acid residues within the linker to both chromophores (uracil–triazole and pyrene). Notably, the pyrene bands exhibit particularly strong intensity, despite the aromatic unit being separated from the chiral center by a long and flexible aliphatic chain. This observation aligns well with the previously described fluorescence properties of the compounds. It can be rationalized by intramolecular π–π stacking interactions between the pyrene and uracil–triazole moieties, whereby the chiral linker dictates the spatial arrangement of the transition dipole moments of the aromatic units, ultimately determining the overall CD spectral profile.

2.3 | Interactions of Tested Ligands with Biorelevant Metal (Cu^{2+}) and Biomolecular Targets: DNA, RNA, and Liposomal Model (POPC MLVs)

2.3.1 | Binding of 2–4 with Cu^{2+} Cation

We have recently demonstrated that triazole can efficiently replace histidine in cation-binding peptides (e.g., Figure 3, **Pyr-Trp**)

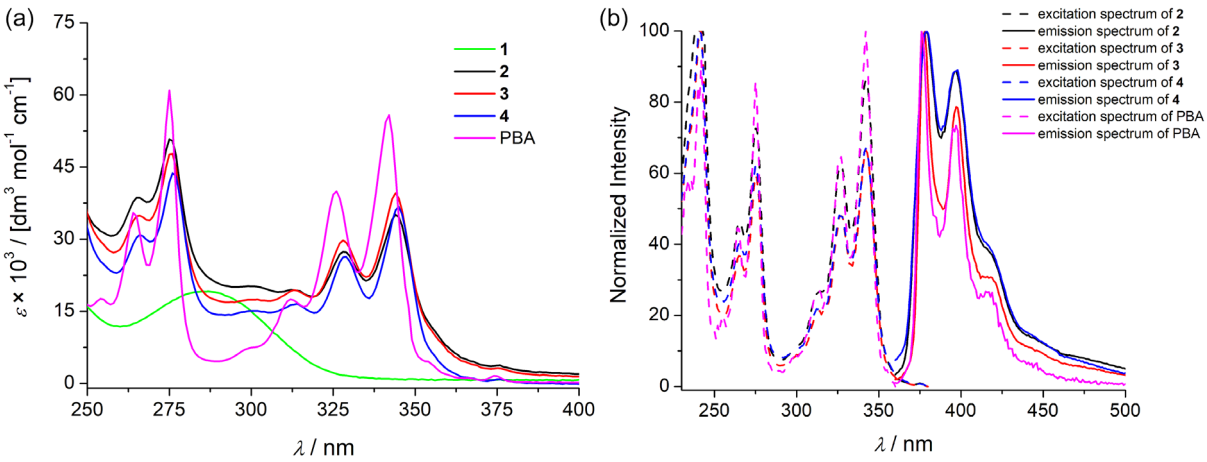

FIGURE 1 | (a) Absorption spectra of **2–4**, references **1** and PBA and (b) normalized excitation (dashed line) and emission (solid line) spectra of **2–4** and PBA ($\lambda_{exc} = 275$ nm, $\lambda_{em} = 397$ nm). Measurements were performed in sodium cacodylate buffer (pH 5.0, $I = 0.05$ M).

14397633, 2026, 8, Downloaded from https://chemistry-europe.onlinelibrary.wiley.com/doi/10.1002/cbic.70312 by Ruder Boskovic Institute, Wiley Online Library on [25/11/2026]. See the Terms and Conditions (https://onlinelibrary.wiley.com/terms-and-conditions) on Wiley Online Library for rules of use; OA articles are governed by the applicable Creative Commons License

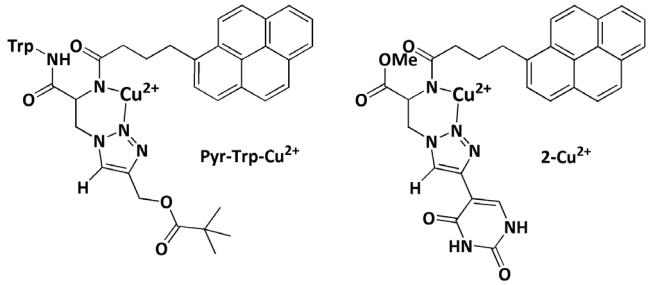

FIGURE 3 | Comparison of Cu^{2+} coordination sites of previously studied analog (**Pyr-Trp**) [36] and ligand **2**.

[7, 52], resulting in short peptides with notable affinity for Cu(II) cations, additionally equipped with DNA-targeting fluorophores for effective monitoring in biorelevant conditions. Here, the studied compounds share a similar structural framework and fluorophore system (Figure 3), but differ in their DNA-recognition element (uracil), which engages in hydrogen-bond-based interactions. For that reason, interactions of novel compounds with the cation Cu^{2+} were examined.

The coordination number and the corresponding binding constant of the copper complexes with individual ligands were determined by titration experiments employing two independent methods. For all pyrene analogs (**2**–**4**), UV/vis titration measurements showed a progressive decrease in absorption intensity upon incremental addition of Cu^{2+} ions (Figures S20a–c and Figure 4). For comparison, UV/vis titration experiments were also conducted with the referent compound **1** (Figure S20d), which lacks the pyrene chromophore and thus shows only a negligible change in the UV/vis spectrum. This allowed assessment of the specific contribution of the pyrene unit to the binding behavior and spectroscopic response upon complexation with Cu^{2+} ions.

For ligand **2**, analysis of the experimental data by global multivariate nonlinear regression analysis performed with the Specfit program (v0.5.0b2) [53, 54] is consistent with a 1:1 ligand–metal coordination mode. In contrast, the sigmoidal profile of the titration data for ligand **3** (Figure S20b) indicates the presence of multiple complex species. The best fit to the Specfit model was obtained when considering the formation of both 2:1 and 1:1 complexes of **3**–Cu^{2+}. The similar values of K_s (1:1) and K_s (2:1) for ligand **3** (Table 2) can be attributed to the involvement of two coordination bonds between molecule **3** and Cu^{2+} cation. Under ligand excess, the 2:1 stoichiometry is favored, whereas under Cu^{2+} excess, the 1:1 complex predominates. When comparing the binding constants of the 1:1 complexes for **2**–Cu^{2+} and **3**–Cu^{2+}, the values obtained from the multivariate analysis of UV/vis titration data are of the same order of magnitude (Table 2) but lower than

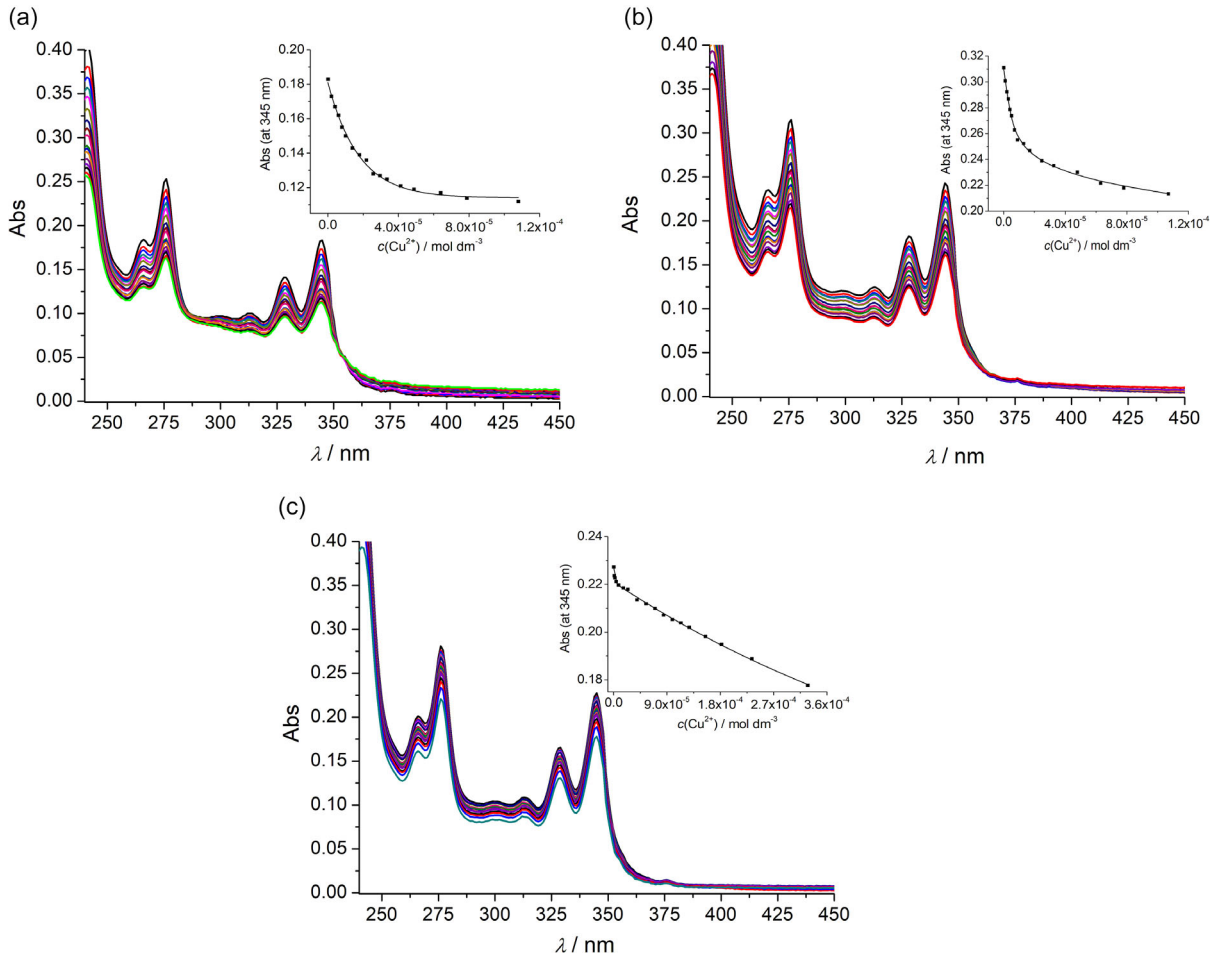

FIGURE 4 | UV/vis titrations with $CuCl_2$ ($c = 2 \times 10^{-3}$ M): (a) **2** ($c = 1 \times 10^{-5}$ M). Inset: dependence of absorbance intensity at $\lambda_{max} = 345$ nm on $c(Cu^{2+})$; (b) **3** ($c = 1 \times 10^{-5}$ M), inset: dependence of absorbance intensity at $\lambda_{max} = 344$ nm on $c(Cu^{2+})$; and (c) **4** ($c = 1 \times 10^{-5}$ M), inset: dependence of absorbance intensity at $\lambda_{max} = 345$ nm on $c(Cu^{2+})$. Measurements were performed in water.

14397633, 2026, 8, Downloaded from https://chemistry-europe.onlinelibrary.wiley.com/doi/10.1002/cbic.70312 by Ruder Boskovic Institute, Wiley Online Library on [25/11/2026]. See the Terms and Conditions (https://onlinelibrary.wiley.com/terms-and-conditions) on Wiley Online Library for rules of use; OA articles are governed by the applicable Creative Commons License

TABLE 2 | Binding constants ([a]log K_s) for 1–4, compared with references 1 and 4' [14] and Pyr-Trp [36] upon titration with Cu^{2+} ($CuCl_2$). Measurements were performed in water.

Compound	1	2	3	4	4′	Pyr-Trp
UV/vis	—[e]	5.1 ± 0.1[b]	5.7 ± 0.2[b] 5.8 ± 0.3[c]	—[d]	/	/
Fluorimetric	/	4.3 ± 0.1[b]	4.5 ± 0.1[b] 7.2 ± 0.2[f]	7.0 ± 0.3[b] 7.0 ± 0.3[c]	5.3 ± 0.04[b]	6.9[g]

[a]UV titrations were based on 16–18 data points and fluorimetric titrations on 9–16 data points; data were processed by multivariate nonlinear regression using Specfit (v0.5.0b2) [53, 54]. The reported error represents the deviation of the fitted curve from the experimental values.
[b]log Ks_{11} for complex stoichiometry **ligand**:Cu = 1:1.
[c]log Ks_{21} for complex stoichiometry **ligand**:Cu = 2:1.
[d]A linear absorption decrease was observed upon adding Cu^{2+}.
[e]No absorption change was observed upon adding Cu^{2+}.
[f]log Ks_{12} for complex stoichiometry **ligand**:Cu = 1:2.
[g]Determined at pH = 7.0 [36].

those determined by fluorimetric titration for the previously studied pyrene analog (Figure 3, left) [36]. The experimental titration data of ligand **4** with the metal ion show a progressive, approximately linear decrease in absorbance over a broad concentration range (Figure S20c), which precludes precise determination of the binding constant of the resulting complex.

As a significantly more sensitive and independent method for assessing the affinity of the investigated ligands toward copper coordination, fluorescence spectroscopy was employed. Nonlinear regression analysis of ligand **2** titrated with an aqueous $CuCl_2$ solution confirmed a 1:1 ligand–metal coordination mode yielding a somewhat lower binding constant than that obtained from spectrophotometric titration (Table 2, Figure S21a), consistent with the differences in method sensitivity. The emission of ligand **3** was also quenched (Figure S21b); however, global fitting analysis of the titration data revealed the formation of two distinct complex species. The binding constant values of the 1:1 complex are comparable for both the **2**–Cu^{2+} and **3**–Cu^{2+} systems (log K_s 4.3 vs. 4.5, respectively). In contrast, the experimental data for the **3**–Cu^{2+} system indicate the presence of an additional 1:2 complex, characterized by a binding constant approximately twice that of the corresponding 1:1 complex. For ligand **4,** the fluorimetric data allowed a reliable determination of the complex binding constants and confirmed formation of both 2:1 and 1:1 **4**–Cu^{2+} stoichiometries (Figure S21c). Intriguingly, the value of K_s (1:1) obtained for **4** was much higher than that of **2** or **3**, and almost identical to the affinity of previously studied **Pyr-Trp** [36], which can eventually be attributed to the contribution of the lysine amino group of **4**, which is lacking in **2** or **3**. Additionally, the Cu(II) binding affinity of the phenanthridine derivative **4′** was examined (Table 2, Figure S21d), showing two orders of magnitude lower binding constant in comparison to pyrene analog **4**. Such a large difference suggests an essential impact of the larger aromatic surface of pyrene, likely by intramolecular stacking interactions preorganizing the cation binding site in a favorable conformation.

CD spectroscopy revealed that coordination with copper markedly influences the chiral properties of the investigated ligands (Figure 5), with the magnitude of this effect being dependent on the length of the chiral bridge connecting the chromophoric units. Ligand **2** (dipeptide) exhibited strong chiral alterations around the pyrene absorption band (Figure 5a, ~345 nm), while ligand **3** (tripeptide) showed chiral changes mostly in the pyrimidine–triazole region (Figure 5b, <300 nm) due to greater flexibility and separation of chromophores. Ligand **4** (tetrapeptide) displayed only slight chiral changes upon copper coordination (Figure 5c), although it demonstrated the strongest metal-binding affinity (log $K_s \geq 7$, Table 2).

The reference ligand **1**, which contains only the pyrimidine–triazole chromophore, exhibits no significant intrinsic CD signal, nor does its spectrum show any noticeable change upon addition of the cation (Figure S22). Taken together, these findings indicate that for **2**–**4** ligand series, a longer, and thus more flexible, chiral bridge results in weaker CD spectra (Figure 2) and Cu-coordination additionally decreases CD spectra intensity (Figure 5), likely due to the planarization of the complex (Figure 3).

2.3.2 | Interactions of Tested Ligands 2–4, and Their Cu(II)-Complexes with Selected Polynucleotides (*ct*DNA, Poly rA–poly rU, Poly(U), and Poly rAH^+–polyrAH^+)

2.3.2.1 | Fluorimetric Titrations of Free Ligands with Polynucleotides. The spectral characteristics of the ligand/Cu(II) complexes and their binding constants (see Chapter 2.3.1) were utilized to evaluate the binding affinities of these complexes toward polynucleotides. For direct comparison, analogous titrations were also performed using the free ligands to assess their binding behavior with the various DNA/RNA double-stranded polynucleotides (*ct*DNA and poly rA–poly rU). Drawing on previous reports of structural analogs exhibiting affinity for uracil-containing RNA [14], the probes were further evaluated against poly(U) homopolymer and, for comparative purposes, poly(A) homopolymer.

The pronounced fluorescence and favorable Stokes shifts of the investigated compounds allowed titrations to be carried out at the low ligand concentration (2 μM). The results processed by nonlinear fitting procedure to Scatchard equation [55–57] show a similar and relatively high (micromolar) affinity of the compounds tested for *ct*DNA (log $K_s = 6–7$) (Figures S23, S27, and S31, Figure 6a, and Table 3), used as a model double-stranded helix and as a baseline for evaluating each ligand's binding potential. Additionally, the formation of complexes between the compounds and *ct*DNA was associated with fluorescence quenching, a phenomenon consistently observed for all three ligands examined. Most calculations yielded a binding ratio of $n = 0.2 \pm 0.05$ (n = [bound dye] / [polynucleotide]). For consistency, all K_s values were recalculated with $n = 0.2$ fixed. The resulting K_s values showed excellent correlation coefficients (> 0.99).

14397633, 2026, 8, Downloaded from https://chemistry-europe.onlinelibrary.wiley.com/doi/10.1002/cbic.70312 by Ruder Boskovic Institute, Wiley Online Library on [25/11/2026]. See the Terms and Conditions (https://onlinelibrary.wiley.com/terms-and-conditions) on Wiley Online Library for rules of use; OA articles are governed by the applicable Creative Commons License

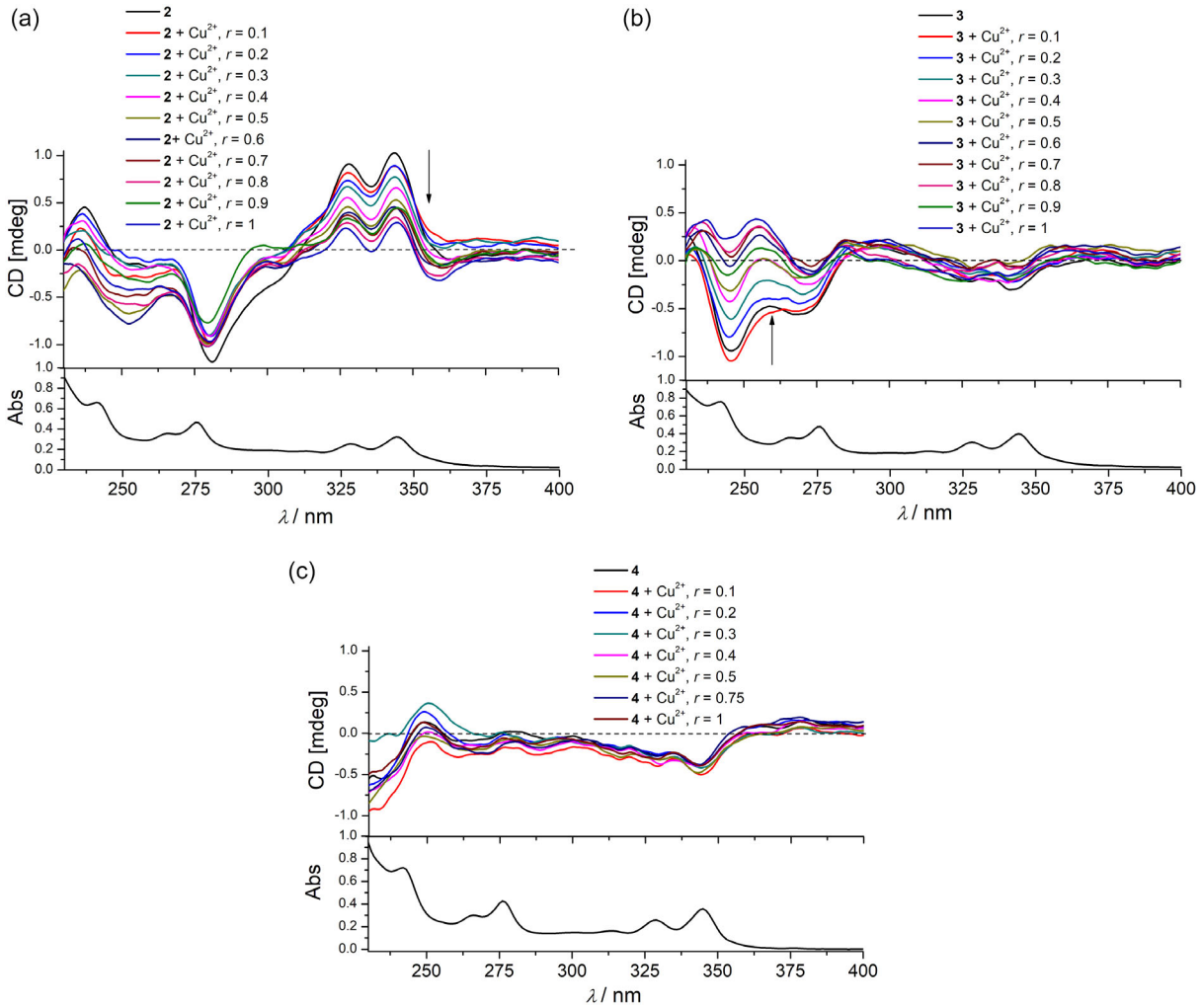

FIGURE 5 | CD titration of: (a) **2**, (b) **3**, and (c) **4** (c(**ligand**) = 1×10^{-5} M) with $CuCl_2$ ($c = 1 \times 10^{-2}$ M) at molar ratio $r = [Cu^{2+}]$ / [compound] 0.1–1.0. Measurements were performed in water.

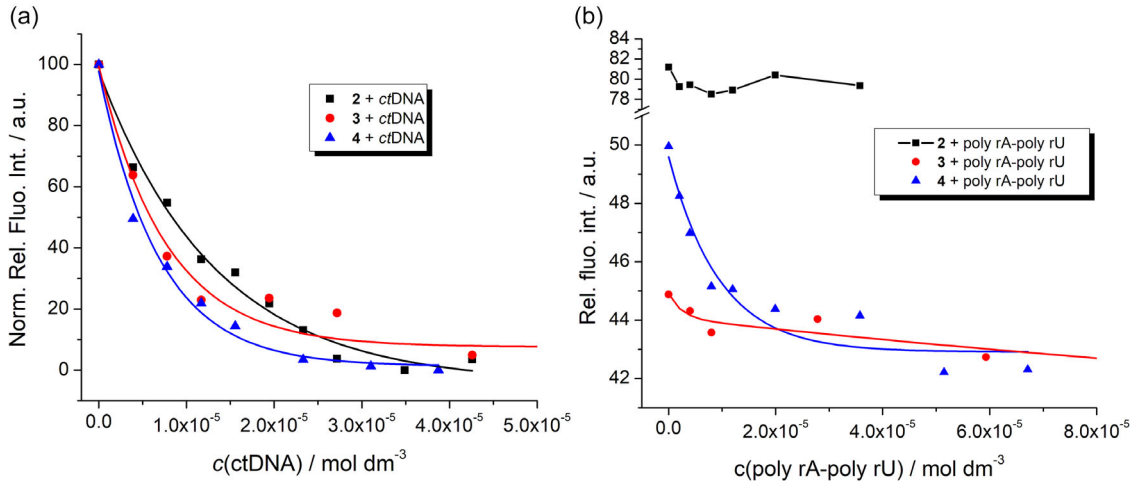

FIGURE 6 | Fluorimetric titration of **2**–**4** (c(ligand) = 2×10^{-6} M, λ_{exc} = 344 nm) with: (a) *ct*DNA and (b) poly rA–poly rU. Fluorescence changes are presented as a function of polynucleotide concentration at the emission maximum (λ_{em} = 397 nm). Measurements were performed in sodium cacodylate buffer (pH 5.0, I = 0.05 M).

When it comes to binding affinity to double-stranded RNA, specifically poly rA–poly rU as a model A-form helix, only tetrapeptide **4** displayed a clear and strong (micromolar) affinity (log $K_s > 6$) (Figure S33, Figure 6b, and Table 3), highlighting the role of the extra positive charge in binding. Conversely, ligands with shorter peptide linkers demonstrated minimal affinity (Figures

14397633, 2026, 8, Downloaded from https://chemistry-europe.onlinelibrary.wiley.com/doi/10.1002/cbic.70312 by Ruder Boskovic Institute, Wiley Online Library on [25/11/2026]. See the Terms and Conditions (https://onlinelibrary.wiley.com/terms-and-conditions) on Wiley Online Library for rules of use; OA articles are governed by the applicable Creative Commons License

TABLE 3 | Binding constants ([a]log K_s) and emission change ([b]ΔInt, in parentheses) for 2–4, previously studied analogs 3′ and 4′ [14] (Scheme 1), and reference pyrene peptide Pyr-Trp [36] (Figure 3) with polynucleotides, determined fluorimetrically. Measurements were performed in sodium cacodylate buffer (pH = 5.0, I = 0.05 M).

	*ct*DNA	poly rA–poly rU	poly rAH$^+$–poly rAH$^+$	poly U
2	5.9 ± 0.10 (0.84)	—[c]	—[c]	—[c]
2–Cu^{2+}	7.5 ± 0.04 (0.75)	7.2 ± 0.07 (0.74)	/	/
3	6.9 ± 0.10 (0.87)	—[c]	4.8 ± 0.03 (0.84)	—[c]
3–Cu^{2+}	5.5 ± 0.20 (0.92)	—[c]	/	/
4	6.6 ± 0.04 (0.70)	6.4 ± 0.30 (0.85)	5.1 ±0.07 (0.72)	5.6 ± 0.10 (0.89)
4–Cu^{2+}	6.2 ± 0.10 (0.84)	6.9 ± 0.07 (0.79)	/	/
3′ [14]	4.5 ± 0.01 (1.70)	5.3 ± 0.01 (0.77)	5.2 ± 0.09 (2.91)	—[c]
4′ [14]	5.3 ± 0.01 (2.91)	6.2 ± 0.01 (3.14)	5.4 ± 0.04 (3.00)	6.0 ± 0.01 (1.29)
Pyr-Trp [36]	6.5 ± 0.10 (0.77)	6.8 ± 0.10 (0.33)	/	/
Pyr-Trp-Cu^{2+} [36]	(5–6) ± 0.08	(5–6) ± 0.08	/	/

[a]Calculated by processing fluorimetric titration data using the Scatchard equation [55–57]. The correlation coefficients are >0.99 for all calculated K_s, and the Scatchard ratios n = [bound dye] / [polynucleotide] are $n = 0.2 \pm 0.05$. For consistency, all K_s values were recalculated with $n = 0.2$, fixed. The standard deviation of the Scatchard equation nonlinear fitting of at least two independent titration experiments is <±0.3.
[b]$\Delta Int = Int_{(100\%\ complex)}/Int_0$.
[c]Fluorescence changes were too small for accurate calculation of the binding constant.

S25, S29, Figure 6b, and Table 3), indicating that both the length and flexibility of the chiral bridge are crucial for selectively recognizing this RNA motif. These results are further supported by the moderate binding affinity of the lysine derivative **4** for poly(U) (log $K_s = 5.6$) (Figure S34, and Table 3) and poly rAH$^+$–poly rAH$^+$ (Figure S32 and Table 3) compared to the other compounds tested (Figures S24, S26, S28, and S30). Comparison of binding constants with previously studied phenanthridine analogs **3**′ and **4**′ (Scheme 1) revealed somewhat higher binding affinity of pyrene analogs for *ct*DNA and poly rA-poly rU, suggesting the impact of the larger aromatic surface of pyrene. Intriguingly, both lysine analogs (**4** and **4**′) showed unexpectedly high affinity toward poly(U), which supports previously mentioned [14] bis-intercalation into poly(U) of phenanthridinium (**4**′) or pyrene(**4**) unit, both equipped with an adequately long and flexible chain.

2.3.2.2 | Fluorimetric Titrations of Ligand–copper(II) Complexes (2–Cu^{2+}, 3–Cu^{2+}, and 4–Cu^{2+}) with Polynucleotides. Furthermore, fluorimetric experiments on the **ligand**–Cu(II) complexes were conducted to compare the initial affinities of the ligands themselves. The **ligand**–Cu(II) complexes were prepared by adding to the ligand solution a 10-fold excess of Cu^{2+}, ensuring formation of > 90% of **ligand**–Cu(II) complex. The excess of Cu^{2+} cations (not bound to ligand) could eventually interact with the polyanionic DNA/RNA backbone, but this would not affect ligand fluorescence.

The addition of selected ds-DNA or ds-RNA to the studied **ligand**–Cu(II) complexes resulted in significant quenching of their emission (Figure 7; Figures S39–S44). The titration data were analyzed using a nonlinear fitting procedure based on the Scatchard equation [55–57], yielding the corresponding binding constants (Table 3).

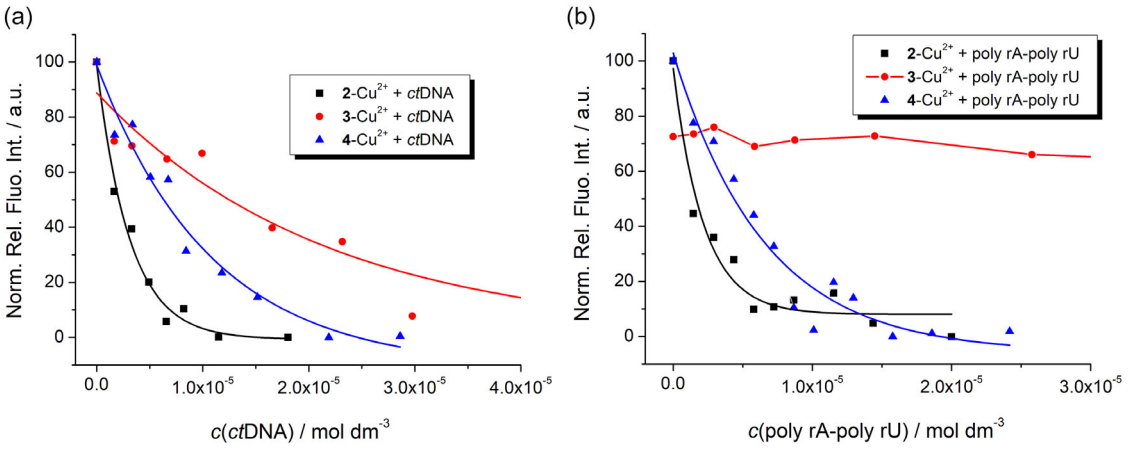

FIGURE 7 | Fluorimetric titration of **2**–Cu^{2+}, **3**–Cu^{2+}, and **4**–Cu^{2+} complexes (c(**ligand**) = 2 × 10^{-6} M, $c(CuCl_2) = 2 \times 10^{-5}$ M, λ_{exc} = 344 nm) with: (a) *ct*DNA and (b) poly rA–poly rU. Fluorescence changes are presented as a function of polynucleotide concentration at the emission maximum. Measurements were performed in sodium cacodylate buffer (pH 7.0, I = 0.05 M).

14397633, 2026, 8, Downloaded from https://chemistry-europe.onlinelibrary.wiley.com/doi/10.1002/cbic.70312 by Ruder Boskovic Institute, Wiley Online Library on [25/11/2026]. See the Terms and Conditions (https://onlinelibrary.wiley.com/terms-and-conditions) on Wiley Online Library for rules of use; OA articles are governed by the applicable Creative Commons License

Analysis of the binding constants (Table 3), which directly reflect the binding affinities of the tested ligands and their copper complexes toward the investigated polynucleotides, revealed pronounced and systematic differences between the free ligands and their metal-bound forms. In particular, the **2**/ctDNA (log $K = 5.9$) vs. **2**–Cu^{2+}/*ct*DNA (log $K = 7.5$) (Figure 8a) and **2**/poly rA–poly rU (lack of measurable change) versus **2**–Cu^{2+}/poly rA–poly rU (log $K = 7.2$) (Figure 8b) systems exhibited markedly altered affinities, highlighting that copper coordination significantly modulates the ligand's interaction with nucleic acids.

Although ligand **2** exhibits a *ct*DNA-binding affinity roughly one order of magnitude lower than ligands **3** and **4** (Table 3), the corresponding **2**–Cu^{2+} complex demonstrates two orders of magnitude higher affinity for *ct*DNA compared to the **3**–Cu^{2+} complex, and at least an order of magnitude higher affinity toward *ct*DNA compared to the **4**–Cu^{2+} complex (Table 3). Remarkably, the **2**–Cu^{2+} complex shows clear selectivity toward double-stranded RNA, as indicated by the exclusive emission quenching observed upon binding with poly rA–poly rU. This interaction is further supported by a high binding constant (log $K = 7.2$, Table 3), confirming the strong binding affinity of the complex (Figure 8b). Based on the obtained results, it can be concluded that dipeptide **2** exhibits a unique ability to distinguish between nucleic acid types and their secondary structures, depending on the presence of copper. This metal ion coordination induces structural rigidity and significantly enhances its affinity toward ds-DNA/RNA, as consistently manifested through fluorescence quenching. In contrast, for tripeptide **3**, elongation of the peptide linker between the fluorescent reporters (uracil–triazole and pyrene) alone positively influences binding to *ct*DNA, whereas structural rigidification reduces its affinity; notably, the affinity toward ds-RNA remains negligible regardless of the ligand's state. Concerning derivative **4**, the elongation of the peptide linker, combined with the additional positive charge within the bridge, proves sufficient to achieve at least micromolar affinity toward both ds-DNA (*ct*DNA) and ds-RNA (poly rA–poly rU), while copper coordination exerts only a marginal effect on these binding interactions.

2.3.2.3 | Thermal Denaturation Experiments of Ds-Polynucleotides with 2–4. Thermal denaturation assays are a valuable method for evaluating how small molecules affect the thermal stability of ds-polynucleotide helices [58]. A pronounced increase in melting temperature ($\Delta T_m > 5°C$) is generally indicative of intercalative binding or minor groove interactions [59]. Conversely, negligible or modest stabilization ($\Delta T_m = 0–5°C$) reflects weaker associations, primarily driven by hydrophobic effects with possible contributions from hydrogen bonding and electrostatic forces, typically excluding classical intercalation. To evaluate the influence of the investigated molecules **2–4** on the thermal stability of ds-polynucleotide sequences, thermal denaturation experiments were performed with ctDNA and poly rA–poly rU. Note that poly A-poly U exhibited biphasic thermal denaturation curves; the lower transition was attributed to the poly A-poly U denaturation, upon which poly A at pH 5.0 formed poly rAH^+–poly rAH^+, which melted at a higher transition temperature. Accordingly, the single poly(A) sequence becomes protonated and adopts a double-stranded conformation (poly rAH^+–poly rAH^+), allowing the experiments to be conducted with all three polynucleotides [42, 43].

Thermal melting experiments revealed that pyrene-conjugates **2–4** generally exerted negligible effects on the stability of double-stranded helices (Table 4; Supplementary Information: Figures S35–S37), similarly to phenanthridine analogs [14] (**3′** or **4′**, Scheme 1). However, for the poly rAH^+–poly rAH^+ sequence, derivatives **2** and **3** exhibited a modest stabilizing effect.

The observed an enhancement in the thermal stability of poly(A) by derivatives **2** and **3**, which can be rationalized by specific interactions at key sites within the helix, rather than a uniform increase in overall binding affinity. Under acidic conditions, protonation of the poly(A) strand likely promotes conformational features that are preferentially stabilized by these derivatives. As a result, even limited binding events can substantially reinforce local helical structure, leading to measurable increases in melting temperature (ΔT_m), despite modest binding constants (log K_s, Table 3). This phenomenon highlights that thermal stabilization and binding affinity do not always correlate directly, and that site-specific interactions can play a dominant role in modulating helix stability.

To investigate how structural rigidification of the ligands upon copper(II) complexation affects the thermal stability of double-stranded nucleic acid structures, we performed thermal

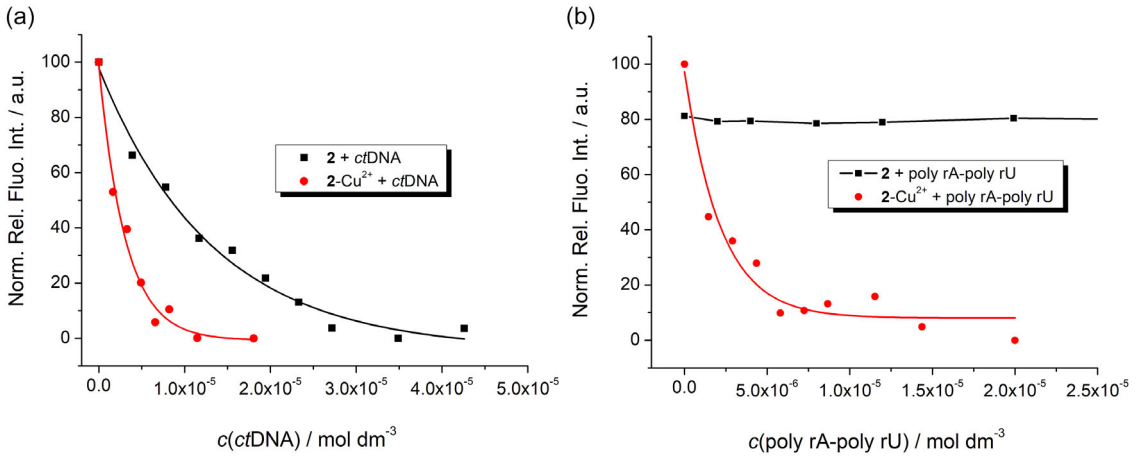

FIGURE 8 | Fluorimetric titration of **2** and **2**–Cu^{2+}complex ($c = 2 \times 10^{-6}$ M, $\lambda_{exc} = 344$ nm) with: (a) *ct*DNA and (b) poly rA–poly rU. Fluorescence changes are presented as a function of polynucleotide concentration at the emission maximum. Measurements were performed in sodium cacodylate buffer (pH 7.0, $I = 0.05$ M).

14397633, 2026, 8, Downloaded from https://chemistry-europe.onlinelibrary.wiley.com/doi/10.1002/cbic.70312 by Ruder Boskovic Institute, Wiley Online Library on [25/11/2026]. See the Terms and Conditions (https://onlinelibrary.wiley.com/terms-and-conditions) on Wiley Online Library for rules of use; OA articles are governed by the applicable Creative Commons License

TABLE 4 | The [a]ΔT_m values (°C) of studied ds-polynucleotides upon addition of 2–4, or their cooper complexes 2–Cu^{2+}, 3–Cu^{2+}, and 4–Cu^{2+} (ratio [b]$r = 0.3$ or 0.5). Measurements were performed in sodium cacodylate buffer (pH = 5.0, $I = 0.05$ M).

Compound	*ct*-DNA	poly rA–poly rU	poly rAH$^+$–poly rAH$^+$
2	−1.1[d]	0/0[c,d]	2.1[d]
	−1.6[e]	0/0[c,e]	
2–Cu^{2+}	−1.1[d]	0/0[c,d]	0.0[d]
3	−1.1[d]	0/0[c,d]	2.0[d]
3–Cu^{2+}	3.7[d]	0.5/1.0[c,d]	2.5[d]
4	0[d]	−0.6/0[c,d]	0.7[d]
4–Cu^{2+}	4.3[d]	0.7/0.5[c,d]	1.3[d]

[a]$\Delta T_m = T_{m\ (poly+compound)} - T_{m\ (poly)}$ (error in $\Delta T_m \pm 0.5$°C).
[b]r = [compound] / [polynucleotide].
[c]Biphasic transitions: the first transition at $T_m = 47$°C is attributed to denaturation of poly rA, poly rU, and the second transition at $T_m = 69$°C is attributed to denaturation of poly rAH$^+$–poly rAH$^+$ since poly rA at pH = 5 is mostly protonated and forms ds-polynucleotide.
[d]$r = 0.3$.
[e]$r = 0.5$.

denaturation (melting) experiments with the corresponding copper complexes (Table 4; Supplementary Information: Figure S38). The **ligand**–Cu complexes were prepared by adding a 10-fold excess of Cu^{2+} to the ligand solution, ensuring formation of > 90% of **ligand**–Cu complex. The excess of Cu^{2+} cations (not bound to ligand) could eventually interact with polyanionic DNA/RNA backbone; thus, we used a control DNA/RNA solution with a matching amount of Cu^{2+} cations added.

The results indicate that coordination of Cu^{2+} to ligand **2** has only a minor impact on the thermal stability of *ct*DNA and the poly rA–poly rU duplex, suggesting that the influence on canonical double-helical structures is minimal or nonperturbative. In contrast, a destabilizing effect was observed for the pseudo-double-stranded poly rAH$^+$–poly rAH$^+$ system, as evidenced by a decrease in melting temperature relative to the free ligand. Compared with the **2**–Cu^{2+} system, **3**–Cu^{2+} and **4**–Cu^{2+} exhibit a markedly stronger influence on the thermal stability of the investigated polynucleotide structures upon coordination with copper(II) ions. The effect is especially evident for *ct*DNA, where an increase in melting temperature of more than 4°C was observed compared to the corresponding free ligands, indicating a notable stabilizing interaction between the copper complexes and the double-helical DNA structure. Stabilizing effects were also detected for the poly rA–poly rU and poly rAH$^+$–poly rAH$^+$ systems; however, these were considerably weaker in magnitude relative to those observed for *ct*DNA.

2.3.2.4 | **Circular Dichroism Spectroscopy.** As an additional, independent approach to gain structural insight into dye interactions with various ds-DNA/RNA and ss-homopolymers, CD spectroscopy was employed. This technique is particularly suitable as it provides valuable structural information based on the electric and magnetic transition moments of adjacent chromophores and their relative orientation. The binding of small molecules can modify the helical chirality of the polynucleotides (<300 nm) or generate induced CD signals at the absorption bands of the ligands. These spectral changes provide insight into the binding mode, including intercalation, groove binding, or aggregation [60, 61].

Considering the inherent chirality of the investigated ligands (Figure S19), changes in the CD spectra of DNA/RNA attributable solely to ligand–polynucleotide binding could, in principle, be obtained by mathematically subtracting the intrinsic CD spectrum of the free ligand from that of the DNA/RNA. However, such an interpretation is not entirely reliable, as the observed spectral changes may arise from multiple factors, including structural alterations of the ligand induced by polynucleotide interaction (which can modify the ligand's inherent chirality) or the formation of exciton coupling between aggregated ligand molecules within the binding site. To obtain a more accurate insight into the type of interaction between each ligand and the examined polynucleotide [60], the experimental CD titration data (where applicable) were analyzed using multivariate nonlinear analysis with the Specfit program (v0.5.0b2) [53, 54]. The binding constants (K_s) used in this analysis were constrained to values independently determined from fluorimetric titration experiments (Table 3). Calculated CD spectra were then compared to the sum of the CD spectra of DNA/RNA and ligand (Figure 9).

As can be concluded from the analysis results (Table S5), the changes in CD spectra are generally neither pronounced nor specific for any of the ligand–polynucleotide combinations and mostly manifest as minor deviations in the helical structure of the polynucleotide itself, particularly in titration experiments with all investigated ligands and *ct*DNA, poly rA–poly rU, and poly(dAdT)$_2$. Comparison of the experimental and mathematically reconstructed spectra also revealed weak induced CD (ICD) signals with a positive sign in the titration experiments of **2**/poly rA–poly rU, **2**/poly(dAdT)$_2$, and **2**/poly(U), although fluorimetric titrations do not support the notion of a significant affinity of ligand **2** for these polynucleotides. Taken together, the results suggest that although fluorimetric data indicate at least micromolar binding affinity of the investigated ligands toward, for example, ctDNA (Table 3), the negligible thermal (de)stabilization (Table 4) and minimal CD spectral changes most likely reflect ligand interactions within the grooves of polynucleotides, mostly based on hydrophobic and electrostatic interactions, which do not significantly alter chirality of ligand or DNA/RNA.

2.3.3 | Interactions of Studied Probes with POPC MLVs

POPC multilamellar vesicles (MLVs) as a POPC-based lipid bilayer biomimetic membrane system serve as an effective model for studying biological membranes. The experiments were conducted under conditions closely resembling physiological environments, using an aqueous buffer (pH 7.0, $I = 0.05$ M). Probes **2**–**4** displayed identical spectrophotometric characteristics in both phosphate buffer and pure water. Excitation at $\lambda_{exc} = 275$ nm, corresponding to a narrow absorption band with high peak intensity, was selected, as this wavelength is well-defined for all three compounds examined.

Preliminary investigations of the interactions between the studied compounds and POPC MLVs demonstrated that binding to the POPC lipid bilayer led to an increase in fluorescence emission for all three compounds. Notably, the extent of this emission enhancement decreased proportionally with the elongation of the peptide linker connecting the two fluorescent reporters (uracil–triazole and pyrene).

14397633, 2026, 8, Downloaded from https://chemistry-europe.onlinelibrary.wiley.com/doi/10.1002/cbic.70312 by Ruder Boskovic Institute, Wiley Online Library on [25/11/2026]. See the Terms and Conditions (https://onlinelibrary.wiley.com/terms-and-conditions) on Wiley Online Library for rules of use; OA articles are governed by the applicable Creative Commons License

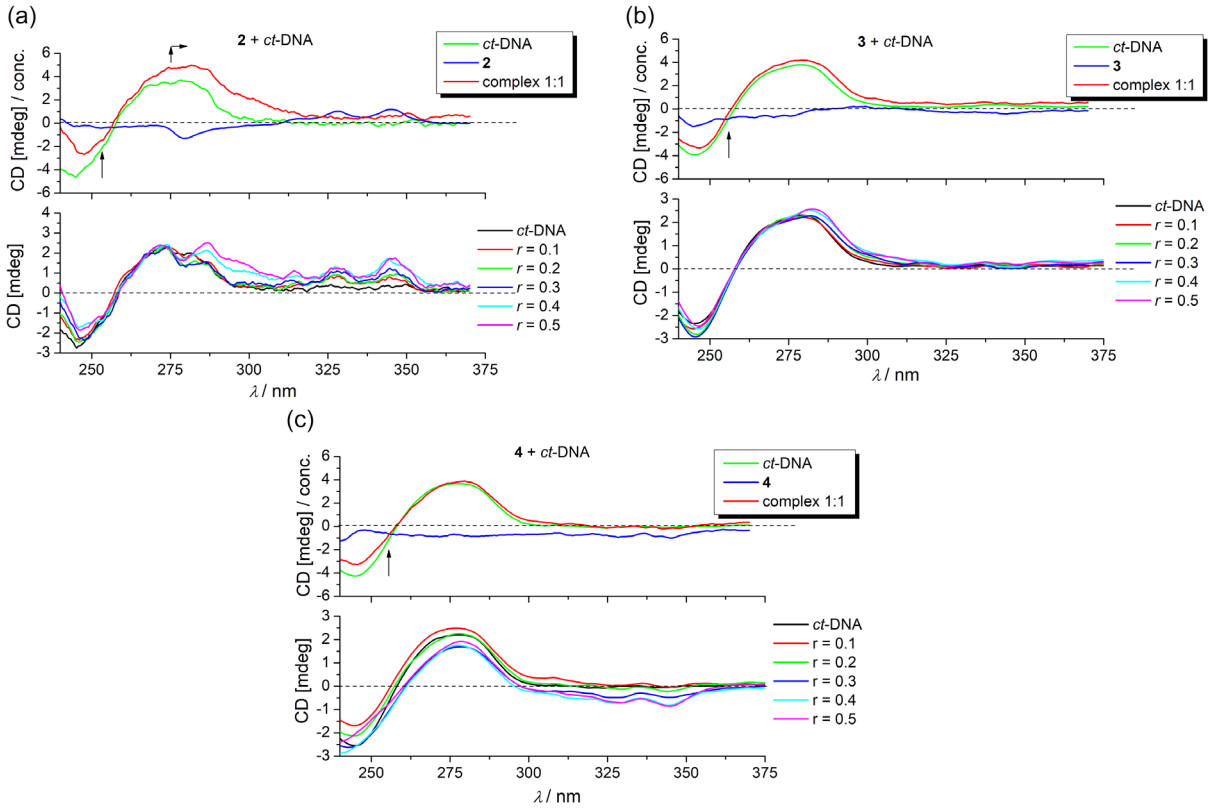

FIGURE 9 | Changes in the CD spectrum of *ct*DNA upon addition of **dye** (c(polynucleotide) = 3×10^{-5} M) at different molar ratios r = [compound] / [polynucleotide] for: (a) ligand **2**, (b) ligand **3**, and (c) ligand **4**. Measurements were performed in sodium cacodylate buffer (pH 5.0, I = 0.05 M). In each figure, the upper panel shows the results obtained by applying a multivariate fitting model (Specfit) [53, 54], while the lower panel displays the experimental data.

At a concentration of $c = 1 \times 10^{-6}$ M, compound **2** exhibited weak fluorescence with three emission maxima at λ = 379, 397, and 418 nm (Figure 10a). Under the same conditions, the MLV solution alone was nonfluorescent, showing a flat baseline. Remarkably, the addition of POPC suspension to compound **2** produced an immediate and pronounced increase in emission at the same wavelengths (Figure 10b UP), stabilizing within 30 s and remaining essentially unchanged for 1 h. A comparable result was observed when compound **2** was added to preformed POPC MLVs (Figure 10b DOWN), indicating uniform probe–bilayer interactions. Heating the POPC MLVs/**2** system to 50°C caused a slight decrease in fluorescence, which recovered upon cooling to 25°C, closely matching the initial room-temperature signal. The emission remained stable over 1 h, with values after 3 days reflecting those observed immediately postheating. While the colloidal nature of the POPC MLVs/**2** system limits precise

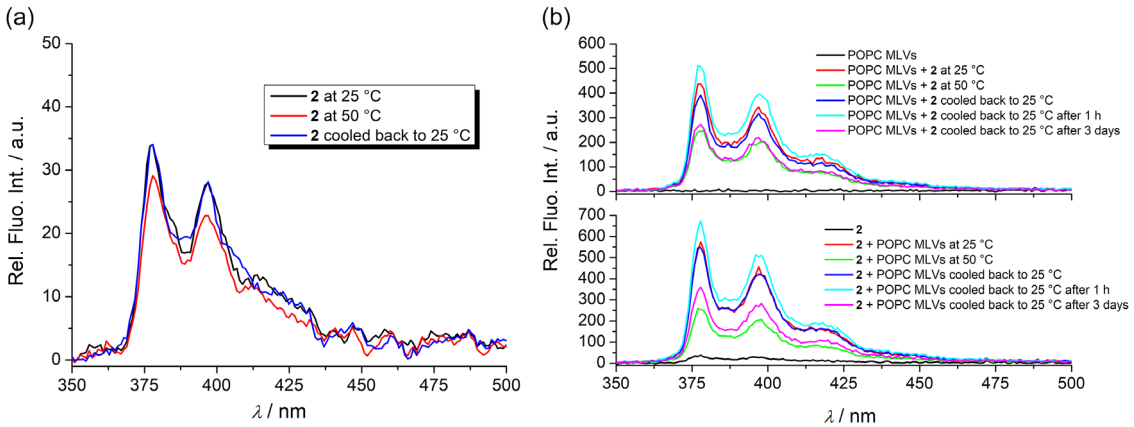

FIGURE 10 | (a) Fluorescence spectrum of **2** ($c = 1 \times 10^{-6}$ M, λ_{exc} = 275 nm, slits 5–5) at room temperature, 50°C, and after cooling down back to room temperature (25°C) and (b) comparison of the fluorescence spectrum of **2** with the emission spectrum of liposome (POPC) (0.125 mg/mL) and mixture of liposome with added **2** at 25°C and upon heating at 50°C and reversible cooling to 25°C. Measurements were performed in phosphate buffer (pH 7.0, I = 0.1 M).

14397633, 2026, 8, Downloaded from https://chemistry-europe.onlinelibrary.wiley.com/doi/10.1002/cbic.70312 by Ruder Boskovic Institute, Wiley Online Library on [25/11/2026]. See the Terms and Conditions (https://onlinelibrary.wiley.com/terms-and-conditions) on Wiley Online Library for rules of use; OA articles are governed by the applicable Creative Commons License

quantum yield determination, qualitative and comparative analyses clearly demonstrate enhanced photophysical behavior upon membrane association—a key feature for biological applications requiring selective localization and high signal-to-noise ratios.

The marked rise in radiative relaxation for **2** upon binding to POPC MLVs, exceeding a 1400% increase in emission, indicates a strong interaction between the conjugate and the membrane environment (Figure 10). Mechanistically, two primary factors are proposed to account for these fluorescence changes. First, a solvatochromic effect likely arises as pyrene is translocated from an aqueous medium into the hydrophobic core of the membrane, resulting in an emission shift and intensity enhancement, characteristic of decreased solvent polarity [62]. Second, membrane interaction appears to induce destacking of the initially intramolecularly folded pyrene-uracil-triazole molecule, disrupting nonradiative quenching pathways and thereby further amplifying fluorescence output. Further supporting this conclusion is the observation that the lifetime of the free ligand cannot be measured due to the weak fluorescence emission of free ligand **2**, whereas experiments with POPC MLVs clearly reveal the presence of a long-lived species (Figure S47). This species provides a compelling explanation for the pronounced increase in the fluorescence intensity of ligand **2** in the POPC MLVs/**2** system. Additionally, the fluorescence quantum yield of the POPC MLVs/**2** system, relative to the reference compound PBA, is approximately three times higher than that of ligand **2** alone (Φ_F(POPC MLVs/**2**) = 0.02 ± 0.005 versus Φ_F(**2**) = 0.006 ± 0.002) (measured in phosphate buffer, pH 7, I = 0.1 M).

Notably, comparative analysis with tripeptide **3** and tetrapeptide **4**, which also interact with POPC MLVs, reveals similar qualitative fluorescence profiles but with substantially reduced emission increases (650% for POPC MLVs/**3** system, and 91% for POPC MLVs/**4** system, see Figures S45 and S46). This trend supports the notion that efficient destacking and quenching alleviation are favored in systems with shorter linkers, as evidenced by the inverse correlation between emission enhancement and linker length. These findings highlight the critical role of linker architecture in modulating both the extent of membrane association and the underlying photophysical mechanisms driving pyrene emission.

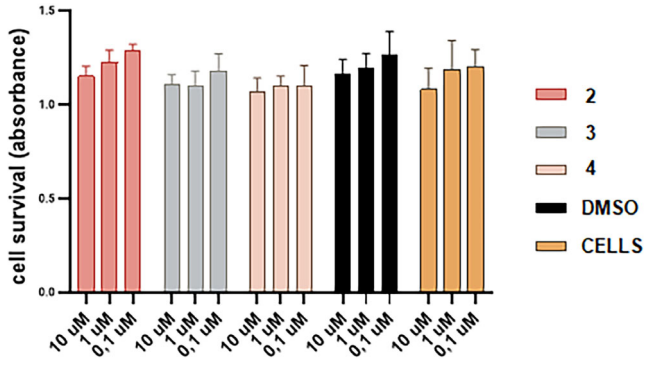

FIGURE 11 | Cell survival of A549 cells treated with different concentrations of studied **dyes** (0.1, 1, and 10 μM). Data are presented as a fold of control cell treated with an amount of DMSO corresponding to DMSO in the tested dyes (<0.1% DMSO in medium), with ± SD from the four replicates in two independent experiments.

3 | Biology

3.1 | Cell Survival of Human Lung Carcinoma Cells Treated with the Investigated Probes 2–4

Previous studies in this work indicated that the investigated dyes strongly bind to ds-DNA/RNA, a feature that could potentially lead to cytotoxicity [63]. To examine their effect on cell viability, the human lung carcinoma cells (A549) were treated with the dyes and assessed using the MTT assay (Figure 11). Compared to DMSO-treated controls, the compounds caused only minimal reductions in cell viability, even at the highest concentration tested (10 μM), indicating low cytotoxicity of the probes **2**-**4** under these conditions.

4 | Conclusion

Building on modular fluorescent sensing reporters, we have developed a novel series of peptidomimetics integrating uracil-triazole with pyrene, a well-established PAH fluorescent chromophore. Incorporating peptide linkers of varying lengths and structural features enabled precise control over the relative orientation and intramolecular organization of the functional modules, which was directly reflected in their photophysical behavior, spectroscopic responses, selectivity, and overall applicability. These observations align and upgrade earlier studies on phenanthridinium (**4′**) and pyrene (**Pyr-Trp**) analogs. Together, these findings reaffirm the versatility of modular design for fine-tuning structure–function relationships in multifunctional fluorescent constructs.

Evaluation of the Cu(II) affinity of the new ligands revealed a pronounced preference for this biologically relevant cation. Clearly resolved CD spectra of the chiral dyes **2**–**4**, supported by UV/vis and fluorimetric titrations, provided definitive evidence of strong metal coordination. Importantly, Cu(II) binding was not only highly dependent on the structural characteristics of the linker but also demonstrated the essential impact of the larger aromatic surface of pyrene with respect to previously studied phenanthridine.

Even between pyrene analogs, there was a difference: the previously studied tryptophan analog **Pyr-Trp** displayed approximately 1000-fold higher affinity for Cu(II) than short and rigid compound **2** (log K_s(**Pyr-Trp**) = 6.9 vs. log K_s(**2**) = 4.3), whereas longer, more flexible linker equipped with additional lysine amino group (**4**) restored high affinity. Pyrene (**4**) proved almost 100-fold more effective than phenanthridine (**4′**) in Cu(II) binding (log K_s(**4**) = 7.0 vs. log K_s(**4′**) = 5.3), underscoring the crucial influence of the extended aromatic surface, most likely through intramolecular stacking interactions that preorganize the cation-binding site into a favorable conformation.

All newly synthesized derivatives exhibited strong interactions with *ct*DNA (micromolar affinity, log K_s = 6–7), and for each system, this binding was noticeably affected upon Cu(II) coordination. The effect was particularly pronounced for compound **2**, whose affinity increased by nearly two orders of magnitude following metal binding (log K_s(**2**) = 5.9 vs. log K_s(**2**–Cu(II)) = 7.5). Notably, the **2**–Cu(II) complex exhibited remarkable selectivity toward the poly rA–poly rU duplex, binding at least an order of magnitude more strongly than its structural analog, the **Pyr-Trp**–Cu(II) complex lacking the uracil unit. This pronounced enhancement highlights the crucial role of the uracil moiety in mediating RNA recognition.

14397633, 2026, 8, Downloaded from https://chemistry-europe.onlinelibrary.wiley.com/doi/10.1002/cbic.70312 by Ruder Boskovic Institute, Wiley Online Library on [25/11/2026]. See the Terms and Conditions (https://onlinelibrary.wiley.com/terms-and-conditions) on Wiley Online Library for rules of use; OA articles are governed by the applicable Creative Commons License

It is plausible that uracil engages in specific hydrogen-bonding interactions with adenine bases in the polynucleotide chain, thereby reinforcing the overall complex stability. Such interactions may involve Hoogsteen-type base pairing, analogous to the U–A–U associations observed in RNA triplex structures [62], effectively contributing an additional level of molecular recognition and sequence discrimination within RNA environments.

The pivotal influence of linker architecture was also evident in studies of derivatives **2**–**4** with POPC-based MLV biomembranes. Noncovalent interaction with POPC MLVs produced remarkable fluorescence enhancements—nearly 100% for **4**, approximately 650% for **3**, and up to 1400% for **2**. Such dependence on linker length supports intramolecular unstacking of the uracil and pyrene, positioning peptide-linked uracil tails inside the membrane for potential recognition by membrane-transporters of short peptides or uracil (mentioned in Introduction) [46, 47]. Also, a strong emission increase is desired for membrane-bioimaging probes. Combined with the negligible in vitro cytotoxicity of all examined compounds, these results strongly encourage further biological evaluation.

Overall, these multifunctional constructs may offer potential for Cu^{2+} binding and sensing, as well as for photo-induced ROS generation under two-photon excitation, which could be relevant for applications such as deep-tissue imaging and localized photodynamic therapy. Combining Cu^{2+} coordination with photochemical ROS production represents a possible strategy for dual-functional theranostic design. Future work will focus on systematically exploring the mechanistic relationships between metal coordination, nucleic-acid recognition, membrane partitioning, and photoactivated cytotoxicity to provide a more comprehensive evaluation of their suitability as multifunctional molecular platforms for biomedical applications.

5 | Experimental Section

5.1 | General

All chemicals and solvents used for the synthesis were analytical or HPLC grade and commercially available. Compound names were generated by ChemDraw Professional (version 20.0.0.41), which follows the IUPAC conventions. Reactions were monitored using thin-layer chromatography (TLC) on silica gel plates (Silica gel 60 F254, Merck, Germany). The compounds were detected on TLC plates under UV light at 254 nm and 365 nm. The products were purified on thin-layer preparative liquid chromatography (Silica gel 60 F254, 1 mm and 2 mm, Merck, Germany). Determination and characterization of product structures was carried out by nuclear magnetic resonance (NMR) and high-resolution mass spectrometry (HRMS). The NMR spectra were recorded on a Bruker Avance III HD 600 MHz/54 mm Ascend equipped with a 5 mm three-channel inversion TCI cryo-probe Prodigy with Z-gradient spiral (model CPP1.1 TCI600S3 H&F-C/N-D-05 Z XT) under the frequency of 300 and 600 MHz (^{1}H) and 75 and 151 MHz (^{13}C) in DMSO–d_6 at room temperature. Tetramethylsilane (TMS) was used as an internal standard. The spectra were processed using MestReNova software, version 0.2–5475, Mestrelab Research S, L; 2009, and analyzed according to one-dimensional (^{1}H and ^{13}C) spectra. Chemical shifts (δ) are expressed according to the residual solvent signal. All chemical shifts are reported in ppm (δ) relative to the internal standards. Signal multiplicities are denoted as s (singlet), d (doublet), t (triplet), q (quartet), and m (multiplet). Coupling constants (J) are given in Hertz. Electrospray ionization (ESI) mass spectra were recorded on the Agilent 6410 Triple Quad mass spectrometer (Agilent Technologies). HRMS were recorded using an Agilent 6540 Q-TOF mass spectrometer (Creative Proteomics, Shirley, NY, USA).

5.2 | General Synthetic Procedure for Coupling Reactions

To a suspension of carboxy-protected amino acid (0.1 mmol) in dry CH_3CN (2 mL), amino-protected amino acid (0.1 mmol) was added in an argon atmosphere. Thereafter, Et_3N (0.2 mmol) was added, followed immediately by HOBT (0.1 mmol) and HBTU (0.1 mmol). The reaction mixture was stirred at room temperature overnight. The solvent was removed under reduced pressure, and the crude material was purified by preparative thin-layer chromatography (CH_2Cl_2/MeOH 9:1) to obtain the desired product, dipeptide or tripeptide.

5.2.1 | 5.2.1. Methyl 3-[4-(2,4-dioxo-1,2,3,4-tetrahydropyrimidin-5-yl)-1H−1,2,3-triazol-1-yl[-2-4-](pyren-1-yl)butanamido]propanoate (2)

Dipeptide **2** was prepared from **A** by applying the **General procedure** in 42% yield. ^{1}H NMR (300 MHz, DMSO–d_6) δ 11.4–11.1 (m, NH-1, NH-3, 2H), 8.6–7.8 (m, C*H-NH-C(O), H6, CH-triazole, 9 × CH-Pyr, 12H), 4.9–4.8 (m, C*H-CH_2, 2H), 4.8–4.7 (m, C*H, 1H), 3.7 (s, OCH_3, 3H), 3.2 (t, J = 7.3 Hz, -CH_2-, 2H), 2.2 (t, J = 6.9 Hz, -CH_2-, 2H), 1.9 (m, -CH_2-, 2H); ^{13}C NMR (75 MHz, DMSO–d_6) δ 172.4 (s, NH-C(O)-$(CH_2)_3$), 169.8 (s, C(O)OCH_3), 162.1 (s, C4), 150.6 (s, C2), 139.0 (s, C-Pyr), 137.7 (d, C6), 136.4 (s, C-triazole), 130.9 (s, C-Pyr), 130.4 (s, C-Pyr), 129.3 (s, C-Pyr), 128.1 (s, C-Pyr), 127.5 (d, CH-Pyr), 127.4 (d, CH-Pyr), 127.2 (d, CH-Pyr), 126.5 (d, CH-Pyr), 126.1 (d, CH-Pyr), 124.9 (d, 2×CH-Pyr), 124.8 (d, CH-Pyr), 124.2 (s, C-Pyr), 124.1 (s, C-Pyr), 123.4 (d, CH-Pyr), 122.7 (d, C-triazole), 103.7 (s, C5), 52.3 (q, OCH_3), 52.3 (d, C(O)-C*H-NH), 49.3 (t, C*H-CH_2-N(triazole)), 34.6 (t, CH_2-(Pyr)), 32.0 (t, CH_2-(Pyr)), 27.3 (t, CH_2-(Pyr)); HRMS: *m/z*: found 551.2043 $[M+H]^+$; calcd. $C_{30}H_{26}N_6O_5 \cdot H^+$: 551.2043.

5.2.2 | 5.2.2. Methyl 3-[4-(2,4-dioxo-1,2,3,4-tetrahydropyrimidin-5-yl)-1H-1,2,3-triazol-1-yl]-2-{2-[4-(pyren-1-yl)butanamido]acetamido}propanoate (3)

Tripeptide **3** was prepared from **1** by applying the **General procedure** in 63% yield. ^{1}H NMR (300 MHz, DMSO–d_6) δ 11.4–11.2 (m, NH-1, NH-3, 2H), 8.5–7.9 (m, 2 × C*H-NH-C(O), H6, CH-triazole, 9 × CH-Pyr, 13H), 4.9–4.8 (m, C*H-CH_2, 2H), 4.7–4.6 (m, C*H, 1H), 3.8–3.7 (m, C(O)-CH_2-NH, 2H), 3.6 (s, OCH_3, 3H), 3.3–3.2 (m, -CH_2-, 2H), 2.3–2.2 (m, -CH_2-, 2H), 2.1–1.9 (m, -CH_2-, 2H); ^{13}C NMR (151 MHz, DMSO–d_6) δ 172.3 (s, NH-C(O)-$(CH_2)_3$), 169.6 (s, C(O)OCH_3), 169.5 (s, NH-C(O)-CH_2), 162.2 (s, C4), 150.7 (s, C2), 139.0 (s, C-Pyr), 137.7 (d, C6), 136.7 (s, C-triazole), 130.9 (s, C-Pyr), 130.5 (s, C-Pyr), 129.3 (s, C-Pyr), 128.2 (s, C-Pyr), 127.6 (d, CH-Pyr), 127.5 (d, CH-Pyr), 127.2 (d, CH-Pyr), 126.5 (d, CH-Pyr), 126.2 (d, CH-Pyr), 125.0 (d, CH-Pyr), 124.9 (d, CH-Pyr), 124.8 (d, CH-Pyr), 124.2 (s, C-Pyr), 124.2 (s, C-Pyr), 123.6 (d, CH-Pyr), 122.9 (d, C-triazole), 103.8 (s, C5), 52.4 (q, OCH_3), 52.3 (d, C(O)-C*H-NH), 49.4 (t, C*H-CH_2-N(triazole)), 41.5

14397633, 2026, 8, Downloaded from https://chemistry-europe.onlinelibrary.wiley.com/doi/10.1002/cbic.70312 by Ruder Boskovic Institute, Wiley Online Library on [25/11/2026]. See the Terms and Conditions (https://onlinelibrary.wiley.com/terms-and-conditions) on Wiley Online Library for rules of use; OA articles are governed by the applicable Creative Commons License

(t, C(O)-CH_2-NH), 34.8 (t, -CH_2-(Pyr)), 32.2 (t, -CH_2-(Pyr)), 27.5 (t, -CH_2-(Pyr)); HRMS: *m/z*: found 608.2263 $[M+H]^+$; calcd. $C_{32}H_{29}N_7O_6{\cdot}H^+$: 608.2258.

5.2.3 | 5.2.3. Methyl 2-{2-[6-(*tert*-butoxycarbonylamino)-2-(4-(pyren-1-yl)butanamido)hexanamido]acetamido}-3-[4-(2,4-dioxo-1,2,3,4-tetrahydropyrimidin-5-yl)-1*H*−1,2,3-triazol-1-yl]propanoate (4boc)

Tetrapeptide **4boc** was prepared from **B** by applying the **General procedure** in 47% yield. ESI-MS: *m/z*: $[M-H]^-$ 834 and $[M+H]^+$ 836.

5.2.4 | 5.2.4. 6-(2-(3-(4-(2,4-dioxo-1,2,3,4-tetrahydropyrimidin-5-yl)-1H-1,2,3-triazol-1-yl)-1-methoxy-1-oxopropan-2-ylamino)-2-oxoethylamino)-6-oxo-5-(4-(pyren-1-yl)butanamido)hexan-1-aminium trifluoroacetate (4)

To a solution of **4boc** (83.6 mg, 0.1 mmol) in CH_2Cl_2 (1 mL), TFA (1 mL) was added. The reaction mixture was stirred at room temperature overnight. Thereafter, the reaction mixture was evaporated under reduced pressure. The oily residue was repeatedly evaporated: first with water (2 × 2 mL), then with methanol (2 × 2 mL), and finally with dichloromethane (2 × 2 mL) to obtain TFA salt **4** in quant. yield (84.9 mg) with no need for further purification. ^{1}H NMR (300 MHz, DMSO–d_6) δ 11.5–11.4 (m, NH-3, 1H), 11.3–11.2 (m, NH-1, 1H), 8.5–7.9 (m, CH-Pyr, H6, CH-triazole, 3 × NH, 14H), 7.7–7.6 (m, NH_3, 3H), 4.9–4.6 (m, 2 × C(O)-C*H-NH, C*H-CH_2-N(triazole), 4H), 3.8–3.5 (m, C(O)-CH_2-NH, OCH_3, 5H), 3.4–3.2 (m, CH_2, 2H), 2.8–2.7 (m, CH_2, 2H), 2.4–2.2 (m, CH_2, 2H), 2.1–1.9 (m, CH_2, 2H), 1.7–1.3 (m, 3 × CH_2, 6H); ^{13}C NMR (75 MHz, DMSO–d_6) δ 172.4 (s, NH-C(O)-$(CH_2)_3$), 172.3 (s, C(O)OCH_3), 172.1 (s, NH-C(O)-C*H), 169.5 (s, NH-C(O)-CH_2), 162.1 (s, C4), 150.6 (s, C2), 138.9 (s, C-triazole), 137.6 (d, C6), 136.6 (s, C-Pyr), 130.9 (s, C-Pyr), 130.4 (s, C-Pyr), 129.3 (s, C-Pyr), 128.1 (s, C-Pyr), 127.5 (d, CH-Pyr), 127.4 (d, CH-Pyr), 127.2 (d, CH-Pyr), 126.5 (d, CH-Pyr), 126.1 (d, CH-Pyr), 124.9 (d, 2 × CH-Pyr), 124.8 (d, 2 × CH-Pyr), 124.2 (s, C-Pyr), 124.1 (s, C-Pyr), 123.5 (d, C-triazole), 103.8 (s, C5), 52.3 (q, OCH_3, d, 2 × C(O)-C*H-NH), 51.4 (t, C*H-CH_2-N(triazole)), 49.4 (t, C(O)-CH_2-NH), 41.5 (t, CH_2-NH_3), 34.8 (t, CH_2), 32.2 (t, CH_2), 31.2 (t, CH_2), 27.4 (t, CH_2), 26.6 (t, CH_2), 22.3 (t, CH_2); HRMS: *m/z*: found 736.3207 $[M+H]^+$; calcd. $C_{38}H_{41}N_9O_7{\cdot}H^+$: 736.3207; found 368.6645 $[M+2H]^{2+}$; calcd. $C_{38}H_{41}N_9O_7{\cdot}2H^+$: 368.6643.

5.3 | Photophysical Measurements

Electronic absorption (UV/vis) spectra were recorded using a Varian Cary 100 Bio spectrophotometer (Varian, Inc., Palo Alto, CA, USA). Fluorescence measurements were performed with a Varian Cary Eclipse fluorimeter (Varian, Inc., CA, USA), ensuring that the sample absorbance at the excitation wavelength remained below 0.05 to minimize inner filter effects. CD spectra were recorded on a JASCO J815 spectropolarimeter (JASCO, Tokyo, Japan). All spectrophotometric measurements were carried out at room temperature (25°C) in appropriate quartz cuvettes (Hellma Suprasil QX, path length 1 cm, Müllheim, Germany) with screw caps, using either an aqueous sodium cacodylate buffer (pH = 5.0 or pH = 7.0, I = 0.05 M), phosphate buffer (pH = 7.0, I = 0.1 M), or Milli-Q water.

Polynucleotides were purchased as noted: calf thymus (ct) DNA poly rA–poly rU, poly dGdC – poly dGdC, poly dAdT – poly dAdT, poly r(A), and poly(U) (Sigma Aldrich, St. Louis, MO, USA), and dissolved in sodium cacodylate buffer (I = 0.05 M, pH = 7.0). The presence of a double-stranded helix was confirmed by a single, well-defined transition in the thermal denaturation experiment, giving a T_m value consistent with the literature, as well as by collecting CD spectra of free ds-DNA or ds-RNA, which also matched the literature [56, 58, 59]. To obtain predominantly short (∼100 base pairs), rod-like B-form DNA fragments, the *ct*DNA was further sonicated and filtered through a 0.45 μm membrane filter [63]. The polynucleotide concentration was determined spectroscopically based on the manufacturer's data, expressed as phosphate concentration (equivalent to c(nucleobase)) [45].

Fluorimetric titration experiments were performed by incremental addition of the $CuCl_2$ or polynucleotide stock solution to a solution of the studied dye. The resulting titration data were analyzed using the Specfit program (for $CuCl_2$) or the Scatchard equation (for DNA/RNA polynucleotides) to calculate the binding constants (K_s) and binding stoichiometry. All fits yielded correlation coefficients greater than 0.999, indicating excellent agreement between experimental and model data. CD experiments were conducted by adding aliquots of the compound stock solution into the polynucleotide solution ($c = 2 \times 10^{-5}$ M), and spectra were recorded at a scanning speed of 200 nm/min (averaging three accumulations). In both sets of experiments (fluorimetric and CD titrations), a buffer background was subtracted from each spectrum. Every reported spectrophotometric titration was the average of at least two measurements. Thermal denaturation curves for ds-DNA, ds-RNA, and their complexes with the studied compounds were determined as previously described [56] by following the absorption change at 260 nm as a function of temperature. The absorbance of the ligands was subtracted from every curve, and the absorbance scale was normalized. The T_m values are the midpoints of the transition curves determined from the maximum of the first derivative and checked graphically by the tangent method. The ΔT_m values were calculated by subtracting the T_m of the free nucleic acid from the T_m of the complex. Every ΔT_m value reported herein was the average of at least two measurements. The error in ΔT_m is ±0.5°C.

Relative fluorescence quantum yields (Φ_f) were measured on an Edinburgh FS5 spectrometer (Edinburgh Instruments, Edinburgh, UK). Fluorescence lifetimes (τ) were determined using the same FS5 instrument in time-correlated single-photon counting (TC-SPC) mode, employing an Edinburgh Instruments EPL-340 picosecond pulsed diode laser (λ_{exc} = 341 nm) as the light source. Before all FS5 measurements, compound solutions were purged with argon for 30 min. For TC-SPC measurements, fluorescence signals at 397 nm were collected over 1023 time channels with a time increment of ≈ 50 ps per channel. Fluorescence decays were collected until the peak channel reached approximately 3000 counts. Instrument response functions (IRFs) were obtained by measuring scattered light from a Ludox suspension (colloidal silica in H_2O) at the excitation wavelength of the laser used (λ_{exc} = 341 nm). Sample absorbance at 397 nm was kept below 0.1. Decay data were fitted using a multiexponential reconvolution model in Fluoracle software (Version 2.11.2). Fit quality was assessed via reduced χ^2 values, Durbin–Watson statistics, and visual inspection of weighted and autocorrelated residuals.

14397633, 2026, 8, Downloaded from https://chemistry-europe.onlinelibrary.wiley.com/doi/10.1002/cbic.70312 by Ruder Boskovic Institute, Wiley Online Library on [25/11/2026]. See the Terms and Conditions (https://onlinelibrary.wiley.com/terms-and-conditions) on Wiley Online Library for rules of use; OA articles are governed by the applicable Creative Commons License

All spectrophotometric measurements were carried out at room temperature (25°C) in appropriate quartz cuvettes (Hellma Suprasil QX, path length 1 cm, Müllheim, Germany) with screw caps, using either an aqueous sodium cacodylate buffer (pH 7.0, $I = 0.05$ M) or phosphate buffer (pH 7.0, $I = 0.1$ M). The fluorescence quantum yields (Φ_F) of the probes were calculated using the equation given below. 1-Pyrenebutyric acid (PBA) in sodium cacodylate buffer ($I = 0.05$ M, pH 7) ($\Phi = 0.15$) [36] was used as the standard for the fluorescence quantum yield calculation using the absorption of the test sample. The emission spectral area is obtained in the 320–600 nm region. Dilute solutions ($\sim 1 \times 10^{-6}$ M) were used to minimize the reabsorption effects of the dyes.

$$\boldsymbol{\phi}_S = \boldsymbol{\phi}_r \times (\boldsymbol{F}_S/\boldsymbol{F}_r) \times (\boldsymbol{A}_r/\boldsymbol{A}_S) \times (\boldsymbol{\eta}_S{}^2/\boldsymbol{\eta}_r{}^2)$$

where $\boldsymbol{\phi}_r$ and $\boldsymbol{\phi}_s$ are the quantum yield of reference and sample, respectively, $\boldsymbol{F}_r$ and $\boldsymbol{F}_s$ are the integrated intensities (areas) of standard and sample spectra, η_r and η_s are the refractive indices of the reference and sample solution, $\boldsymbol{A}_r$ and $\boldsymbol{A}_s$ are the absorbance intensities of reference and sample, respectively.

5.4 | POPC MLVs preparation and Experiments

The synthesis of POPC MLVs required for subsequent titration experiments was carried out according to a previously published procedure [64–66] with slight modifications. POPC lipid (1-palmitoyl-2-oleoyl-sn-glycero-3-phosphocholine; 5.27 mg) was dissolved in 3 mL of chloroform ($\gamma = 1.76$ mg/mL) in a round-bottom flask and evaporated using a rotary evaporator. The thin lipid film formed on the flask wall was further dried under a stream of argon and rehydrated with 5.27 mL of phosphate buffer (Na_2HPO_4 and NaH_2PO_4; pH = 7, $I = 0.1$ M; γ(POPC) = 1 mg/mL). After rehydration, the flask was vortexed for 25 s, cooled in liquid nitrogen for 25 s, and heated in a water bath at 40°C for 30 s. This vortex–cooling–heating cycle was repeated five times. The resulting liposome suspension was stored at 4°C.

5.5 | Dynamic Light Scattering (DLS) – Characterization and Data Analysis of POPC MLVs

POPC MLVs solutions ($\gamma = 0.05$ mg/mL) for dynamic light scattering (DLS) and zeta potential measurements were prepared by diluting the POPC MLVs suspension (γ(POPC) = 1 mg/mL) with phosphate buffer (pH = 7.08, $I = 100$ mM). A total of 3.2 mL of the diluted solution was prepared—1 mL for DLS measurements (optimal volume), and 2 mL for zeta potential measurements. The size distribution of the prepared MLVs was established with DLS using a photon correlation spectrophotometer equipped with a 532 nm (green) laser (Zetasizer Nano ZS, Malvern Instruments, Worcestershire, UK). The average hydrodynamic diameter (d_h) was specified as the value at the peak maximum of the volume size distribution. The reported results correspond to the average of three measurements at 25°C. The data processing was conducted by the Zetasizer software 802 (Malvern Instruments). The average hydrodynamic diameter (d_h) value of the POPC MLVs (at γ(POPC) = 0.05 mg mL^{-1}) was 423±24 nm, and zeta potential (ζ) was 7.21 ± 1.28 mV.

Titration experiments were performed by adding an aliquot of POPC MLVs (opalescent solution in phosphate buffer) to the solution of the studied compound. Following initial incubation, changes in the fluorescence emission of the dye upon interaction with POPC MLVs were monitored at room temperature, at 50°C, after cooling back to room temperature, and over time after 1 hour and 3 days of incubation.

5.6 | Biology

5.6.1 | Cells

Commercially available human lung adenocarcinoma A549 cells (ATCC CCL-185) and normal lung fibroblast WI-38 cells (ATCC CCL-75) were obtained from the American Type Culture Collection (ATCC) and cultured in accordance with the manufacturer's protocols. A549 cells were propagated in Dulbecco's Modified Eagle Medium (DMEM, Sigma Aldrich, USA), whereas WI-38 cells were maintained in Eagle's Minimum Essential Medium (EMEM, Sigma Aldrich, USA). Both media were supplemented with 10% fetal bovine serum (FBS, Sigma Aldrich, USA). Cells were incubated at 37°C in a humidified atmosphere containing 5% CO2. All experiments were performed in biological triplicate to ensure reproducibility.

5.6.2 | Cell viability assay

Chemical compounds were dissolved in dimethyl sulfoxide (DMSO, Gram-Mol, Zagreb, Croatia) under sterile conditions to prepare 10 mM stock solutions, which were stored in the dark at 4°C. Fresh working solutions were prepared by diluting the stock solutions in either DMEM or EMEM depending on type of cells, before each assay, ensuring that the final DMSO concentration did not exceed 0.1%. A549 and WI-38 cells were seeded in 96-well plates at a density of 7×10^3 cells per well in 100 µL of DMEM or EMEM, respectively, both supplemented with 10% fetal bovine serum, and incubated overnight at 37°C in a 5% CO2 atmosphere. The following day, 100 µL of the compound working solutions were added to achieve final concentrations ranging from 10 to 0.1 µM. Cells treated with equivalent DMSO dilutions served as controls, while those treated with only DMEM or EMEM (10% FBS) were used as negative controls. After 72 h of incubation, the medium was removed, and 40 µL of MTT reagent was added to each well. Following a 3 h incubation, formazan crystals formed and were dissolved by adding 170 µL of DMSO per well, followed by 20 min of agitation on a shaker. The absorbance of the MTT-formazan product was measured at 600 nm using a microplate reader, with absorbance values corresponding to cell viability. All experiments were performed in biological duplicates and technical quadruplicates.

Acknowledgments

D. P. S. and I. P. gratefully acknowledge the financial support from the Croatian Science Foundation project IP-2022-10–9829. D.P.S. gratefully acknowledges members of the Laboratory for biocolloids and surface chemistry (Division for Physical Chemistry, Ruđer Bošković Institute) for access to the Zetasizer Nano ZS (Malvern).

Funding

This research was funded by the Croatian Science Foundation project HrZZ IP-2022-10-9829.

14397633, 2026, 8, Downloaded from https://chemistry-europe.onlinelibrary.wiley.com/doi/10.1002/cbic.70312 by Ruder Boskovic Institute, Wiley Online Library on [25/11/2026]. See the Terms and Conditions (https://onlinelibrary.wiley.com/terms-and-conditions) on Wiley Online Library for rules of use; OA articles are governed by the applicable Creative Commons License

Conflicts of Interest

The authors declare no conflicts of interest.

Data Availability Statement

The data that supports the findings of this study are available in the supplementary material of this article.

References

1. J. B. Chaires, "A Small Molecule-DNA Binding Landscape," *Biopolymers* 103 (2015): 473.

2. J. L. Childs-Disney, X. Yang, Q. M. R. Gibaut, Y. Tong, R. T. Batey, and M. D. Disney, "Targeting RNA Structures with Small Molecules," *Nature Reviews Drug Discovery* 21 (2022): 736.

3. S. Bhaduri, N. Ranjan, and D. P. Arya, "An Overview of Recent Advances in Duplex DNA Recognition by Small Molecules," *Beilstein Journal of Organic Chemistry* 14 (2018): 1051.

4. J. Lhomme, J. F. Constant, and M. Demeunynck, "Abasic DNA Structure, Reactivity, and Recognition," *Biopolymers* 52, no. 2 (1999): 65.

5. A. Lauria, A. Montalbano, P. Barraja, G. Dattolo, and A. M. Almerico, "DNA Minor Groove Binders: An Overview on Molecular Modeling and QSAR Approaches," *Current Medicinal Chemistry* 14, no. 20 (2007): 2136.

6. A. Rahman, P. O'Sulivan, and I. Rozas, "Recent Developments in Compounds Acting in the DNA Minor Groove," *MedChemComm* 10 (2019): 26.

7. E. K. Carter, S. Laughlin-Toth, T. Dodd, W. D. Wilson, and I. Ivanov, "Small Molecule Binders Recognize DNA Microstructural Variations *via* an Induced Fit Mechanism," *Physical Chemistry Chemical Physics* 21 (2019): 1841.

8. E. N. Ogbonna, J. R. Terrell, A. Paul, et al., "Single GC Base Pair Recognition by a Heterocyclic Diamidine: Structures, Affinities, and Dynamics," *RSC Advances* 14 (2024): 29675.

9. H. S. Haniff, A. Graves, and M. D. Disney, "Selective Small Molecule Recognition of RNA Base Pairs," *ACS Combinatorial Science* 20, no. 8 (2018): 482.

10. A. Taghavi, N. A. Springer, P. R. A. Zanon, et al., "The Evolution and Application of RNA-Focused Small Molecule Libraries," *RSC Chemical Biology* 6 (2025): 510.

11. M. Wang, Y. Yu, C. Liang, A. Lu, and G. Zhang, "Recent Advances in Developing Small Molecules Targeting Nucleic Acid," *International Journal of Molecular Sciences* 17, no. 6 (2016): 779.

12. I. Juranović, Z. Meić, I. Piantanida, L.-M. Tumir, and M. Žinić, "Interactions of Phenanthridinium-Nucleobase Conjugates with Polynucleotides in Aqueous Media. Recognition of Poly U," *Chemical Communications* no. 13 (2002): 1432.

13. M. Radić Stojković, S. Marczi, L. J. Glavaš-Obrovac, and I. Piantanida, "Permanent Positive Charge Strongly Influences DNA/RNA Binding and Antiproliferative Activity of Urea–phenanthridinium Conjugates," *European Journal of Medicinal Chemistry* 45, no. 8 (2010): 3281.

14. D. Saftić, M. Radić Stojković, B. Žinić, et al., "Impact of Linker between Triazolyluracil and Phenanthridine on Recognition of DNA and RNA. Recognition of Uracil-Containing RNA," *New Journal of Chemistry* 41 (2017): 13240.

15. I. Piantanida, S. B. Palm, P. Čudić, M. Žinić, and H.-J. Schneider, "Phenanthridinium Cyclobisintercalands. Fluorescence Sensing of AMP and Selective Binding to Single-Stranded Nucleic Acids," *Tetrahedron Letters* 42, no. 38 (2001): 6779.

16. G. Malojčić, I. Piantanida, M. Marinić, et al., "A Novel Bis-Phenanthridine Triamine with pH Controlled Binding to Nucleotides and Nucleic Acids," *Organic & Biomolecular Chemistry* 3 (2005): 4373.

17. L.-M. Tumir, M. Grabar, S. Tomić, and I. Piantanida, "The Interactions of Bis-Phenanthridinium–nucleobase Conjugates with Nucleotides: Adenine-Conjugate Recognizes UMP in Aqueous Medium," *Tetrahedron* 66, no. 13 (2010): 2501.

18. M. Grabar Branilović, S. Tomić, L.-M. Tumir, and I. Piantanida, "The Bis-Phenanthridinium System Flexibility and Position of Covalently Bound Uracil Finely Tunes the Interaction with Polynucleotides," *Molecular Biosystems* 9 (2013): 2051.

19. L.-M. Tumir, F. Šupljika, and I. Piantanida, "Bis-Phenanthridinium–adenine Conjugates as Fluorescent and CD Reporters for Fine Structural Differences in Ds-DNA/RNA and ss-RNA Structures," *Supramolecular Chemistry* 28, no. 3-4 (2015): 267.

20. L.-M. Tumir, M. Radić Stojković, and I. Piantanida, "Come-Back of Phenanthridine and Phenanthridinium Derivatives in the 21st Century," *Beilstein Journal of Organic Chemistry* 10 (2014): 2930.

21. J. Matić, F. Šupljika, T. Tandarić, et al., "DNA/RNA Recognition Controlled by the Glycine Linker and the Guanidine Moiety of Phenanthridine Peptides," *International Journal of Biological Macromolecules* 134 (2019): 422.

22. T. Šmidlehner, M. Košćak, K. Božinović, D. Majhen, C. Schmuck, and I. Piantanida, "Fluorimetric and CD Recognition between Various Ds-DNA/RNA Depends on a Cyanine Connectivity in Cyanine-Guanidiniocarbonyl-Pyrrole Conjugate," *Molecules* 25, no. 19 (2020): 4470.

23. T. Šmidlehner, A. Rožman, and I. Piantanida, "Advances in Cyanine - Amino Acid Conjugates and Peptides for Sensing of DNA, RNA and Protein Structures," *Current Protein & Peptide Science* 20, no. 11 (2019): 1040.

24. T. Šmidlehner, Z. Karačić, S. Tomić, C. Schmuck, and I. Piantanida, "Fluorescent Cyanine-Guanidiniocarbonyl-Pyrrole Conjugate with pH-Dependent DNA/RNA Recognition and DPP III Fluorescent Labelling and Inhibition Properties," *Monatshefte Fur Chemie* 149 (2018): 1307.

25. J. Matić, L.-M. Tumir, M. Radić Stojković, and I. Piantanida, "Advances in Peptide-Based DNA/RNA-Intercalators," *Current Protein & Peptide Science* 17, no. 2 (2016): 127.

26. Ž. Ban, B. Žinić, R. Vianello, C. Schmuck, and I. Piantanida, "Nucleobase–Guanidiniocarbonyl-Pyrrole Conjugates as Novel Fluorimetric Sensors for Single Stranded RNA," *Molecules* 22, no. 12 (2017): 2213.

27. N. Z. Fantoni, A. H. El-Sagheer, and T. Brown, "A Hitchhiker's Guide to Click-Chemistry with Nucleic Acids," *Chemical Reviews* 121, no. 12 (2021): 7122.

28. M. M. Alam, "1,2,3-Triazole Hybrids as Anticancer Agents: A Review," *Archiv der Pharmazie* 355 (2021): e2100158.

29. C. Deng, H. Yan, J. Wang, K. Liu, B.- S. Liu, and Y.- M. Shi, "1,2,3-Triazole-Containing Hybrids with Potential Antibacterial Activity against ESKAPE Pathogens," *European Journal of Medicinal Chemistry* 244 (2022): 114888.

30. N. Poonia, A. Kumar, V. Kumar, M. Yadav, and K. Lal, "Recent Progress in 1H-1,2,3-Triazoles as Potential Antifungal Agents," *Current Topics in Medicinal Chemistry* 21, no. 23 (2021): 2109.

31. A. Singh, K. Singh, A. Sharma, et al., "1,2,3-Triazole Derivatives as an Emerging Scaffold for Antifungal Drug Development against *Candida albicans*: A Comprehensive Review," *Chemistry & Biodiversity* 20 (2023): e202300024.

32. S. Sirisha, N. Kerru, V. Prasannakumar, et al., "Novel Indole-Linked 1,2,3-Triazole Analogues: Synthesis, Anti-Tubercular Screening, and Molecular Docking Analysis," *Journal of Heterocyclic Chemistry* 62 (2025): 1515.

33. E. Bonandi, M. S. Christodoulou, G. Fumagalli, D. Perdicchia, G. Rastelli, and D. Passarella, "The 1,2,3-Triazole ring as a Bioisostere in Medicinal Chemistry," *Drug Discovery Today* 22, no. 10 (2017): 1572.

14397633, 2026, 8, Downloaded from https://chemistry-europe.onlinelibrary.wiley.com/doi/10.1002/cbic.70312 by Ruder Boskovic Institute, Wiley Online Library on [25/11/2026]. See the Terms and Conditions (https://onlinelibrary.wiley.com/terms-and-conditions) on Wiley Online Library for rules of use; OA articles are governed by the applicable Creative Commons License

34. A. Banasiak, N. Z. Fantoni, A. Kellett, and J. Coleran, "Mapping the DNA Damaging Effects of Polypyridyl Copper Complexes with DNA Electrochemical Biosensors," *Molecules* 27, no. 3 (2022): 645.

35. R. Galindo-Murillo, J. C. García-Ramos, L. Ruiz-Azuara, E. T. Cheatham, and F. Cortés-Guzmán, "Intercalation Processes of Copper Complexes in DNA," *Nucleic Acids Research* 43, no. 11 (2015): 5364.

36. I. Krošl, M. Košćak, K. Ribičić, et al., "Impact of the Histidine-Triazole and Tryptophan-Pyrene Exchange in the WHW Peptide: Cu(II) Binding, DNA/RNA Interactions and Bioactivity," *International Journal of Molecular Sciences* 23 (2022): 7006.

37. H. Kumari, A. Eiseinhart, J. Pajoubpong, F. Heinrich, and T. L. Beck, "Investigating Partitioning of Free versus Macrocycle Bound Guest into a Model POPC Lipid Bilayer," *RSC Advances* 10 (2020): 15148.

38. A. Åkesson, T. Lind, N. Ehrlich, D. Stamou, H. Wacklin, and M. Cárdenas, "Composition and Structure of Mixed Phospholipid Supported Bilayers Formed by POPC and DPPC," *Soft Matter* 8 (2012): 5658.

39. C. R. Cantor and P. R. Schimmel, *Biophysical Chemistry, Vol. 3* (WH Freeman and Co, 1980), 1109.

40. W. Saenger, *Principles of Nucleic Acid Structure* (Springer-Verlag, 1983).

41. J. W. Wojtkowiak, D. Verduzco, K. J. Schramm, and R. J. Gillies, "Drug Resistance and Cellular Adaptation to Tumor Acidic pH Microenvironment," *Molecular Pharmaceutics* 8 (2011): 2032.

42. S. Chakraborty, S. Sharma, P. K. Maiti, and Y. Krishnan, "The Poly dA Helix: A New Structural Motif for High Performance DNA-Based Molecular Switches," *Nucleic Acids Research* 37, no. 9 (2009): 2810.

43. M. L. Gleghorn, J. Zhao, D. H. Turner, and L. E. Maquat, "Crystal Structure of a Poly(rA) Staggered Zipper at Acidic pH: Evidence that Adenine N1 Protonation Mediates Parallel Double Helix Formation," *Nucleic Acids Research* 44, no. 17 (2016): 8417.

44. L. Ma, Q. Ouyang, G. C. Werthmann, H. M. Thompson, and E. M. Morrow, "Live-Cell Microscopy and Fluorescence-Based Measurement of Luminal pH in Intracellular Organelles," *Frontiers in Cell and Developmental Biology* 5 (2017): 71.

45. L.-M. Tumir, I. Piantanida, I. Juranović Cindrić, T. Hrenar, Z. Meić, and M. Žinić, "New Permanently Charged Phenanthridinium–Nucleobase Conjugates. Interactions with Nucleotides and Polynucleotides and Recognition of Ds-PolyAH$^+$," *Journal of Physical Organic Chemistry* 16 (2003): 891.

46. D. E. Smith, B. Clémençon, and M. A. Hediger, "Proton-Coupled Oligopeptide Transporter Family SLC15: Physiological, Pharmacological and Pathological Implications," *Molecular Aspects of Medicine* 34, no. 2-3 (2013): 323.

47. N. J. Wright and S. Y.Lee, "Toward a Molecular Basis of Cellular Nucleoside Transport in Humans," *Chemical Reviews* 121, no. 9 (2021): 5336.

48. N. S. Kumar, M. D. Gujrati, and J. N. Wilson, "Evidence of Preferential Pi-Stacking: A Study of Intermolecular and Intramolecular Charge Transfer Complexes," *Chemical Communications* 46, no. 30 (2010): 5464.

49. J. Matić, T. Tandarić, M. Radić Stojković, et al., "Phenanthridine–pyrene Conjugates as Fluorescent Probes for DNA/RNA and an Inactive Mutant of Dipeptidyl Peptidase Enzyme," *Beilstein Journal of Organic Chemistry* 19 (2023): 550.

50. S. E. Wheeler, "Understanding Substituent Effects in Noncovalent Interactions Involving Aromatic Rings," *Accounts of Chemical Research* 46, no. 4 (2013): 1029.

51. J. Hwang, B. E. Dial, P. Li, M. E. Kozik, M. D. Smith, and K. D. Shimizu, "How Important Are Dispersion Interactions to the Strength of Aromatic Stacking Interactions in Solution?," *Chemical Science* 6 (2015): 4358.

52. M. Košćak, I. Krošl, B. Žinić, and I. Piantanida, "Fluorescent Analogues of FRH Peptide: Cu(II) Binding and Interactions with Ds-DNA/RNA," *Chemosensors* 10 (2022): 34.

53. H. Gampp, M. Maeder, C. J. Meyer, and A. D. Zuberbuhler, "Calculation of Equilibrium-Constants from Multiwavelength Spectroscopic Data—II: SPECFIT: Two User-Friendly Programs in Basic and Standard FORTRAN. 77," *Talanta* 32 (1985): 257.

54. M. Maeder and A. D. Zuberbuhler, "Nonlinear Least-Squares Fitting of Multivariate Absorption Data," *Analytical Chemistry* 62 (1990): 2220.

55. J. D. McGhee and P. H. von Hippel, "Theoretical Aspects of DNA-Protein Interactions: Co-Operative and Non-Co-Operative Binding of Large Ligands to a One-Dimensional Homogeneous Lattice," *Journal of Molecular Biology* 86 (1974): 469.

56. G. Scatchard, "The Attractions of Proteins for Small Molecules and Ions," *Annals of the New York Academy of Sciences* 51 (1949): 660.

57. M. G. Gore, *Spectrophotometry and Spectrofluorimetry. A Practical Aproach* (Oxford University Press, 2000).

58. J. L. Mergny and L. Lacroix, "Analysis of Thermal Melting Curves," *Oligonucleotides* 13 (2003): 515.

59. W. D. Wilson, L. Ratmeyer, M. Zhao, L. Strekowski, and D. Boykin, "The Search for Structure-Specific Nucleic Acid-Interactive Drugs: Effects of Compound Structure on RNA versus DNA Interaction Strength," *Biochemistry* 32 (1993): 4098.

60. T. Šmidlehner, I. Piantanida, and G. Pescitelli, "Polarization Spectroscopy Methods in the Determination of Interactions of Small Molecules with Nucleic Acids - Tutorial," *Beilstein Journal of Organic Chemistry* 14 (2018): 84.

61. M. Eriksson and B. Norden, "Linear and Circular Dichroism of Drug-Nucleic Acid Complexes," *Methods in Enzymology* 340 (2001): 68.

62. J. R. Lakowicz, *Principles of Fluorescence Spectroscopy* (Springer-Verlag US, 2006).

63. M. Demeunynck, C. Bailly, and W. D. Wilson, *Small Molecule DNA and RNA Binders: From Synthesis to Nucleic Acid Complexes* (Wiley-VCH Verlag GmbH & Co. KGaA, 2004).

64. A. Ruszkowska, M. Ruszkowski, J. P. Hulewicz, Z. Dauter, and J. A. Brown, "Molecular Structure of a U•A-U-Rich RNA Triple Helix with 11 consecutive Base Triples," *Nucleic Acids Research* 48 (2020): 3304.

65. J. B. Chaires, N. Dattagupt, and D. M. Crothers, "Studies on Interaction of Anthracycline Antibiotics and Deoxyribonucleic Acid: Equilibrium Binding Studies on the Interaction of Daunomycin with Deoxyribonucleic Acid," *Biochemistry* 21 (1982): 3933.

66. M. Belovari, L. Pašalić, B. Pem, et al., "Search for the Smallest Switch-on, Water Soluble and a Phase-Sensitive Fluorimetric Probe for Lipid Membranes: *N*-Aryl Isoindolin-1-One Core," *Microchemical Journal* 208 (2025): 112335.

Supporting Information

Additional supporting information can be found online in the Supporting Information section.

14397633, 2026, 8, Downloaded from https://chemistry-europe.onlinelibrary.wiley.com/doi/10.1002/cbic.70312 by Ruder Boskovic Institute, Wiley Online Library on [25/11/2026]. See the Terms and Conditions (https://onlinelibrary.wiley.com/terms-and-conditions) on Wiley Online Library for rules of use; OA articles are governed by the applicable Creative Commons License